INORGANIC CHEMISTRY FRONTIERS

RESEARCH ARTICLE

View Article Online
View Journal | View Issue

Cite this: *Inorg. Chem. Front.*, 2026, **13**, 3553

Eu(III) dilution of Er(III) and Yb(III) molecular nanomagnets as a route to improving their magnetic features and creating a link with optical thermometry

Aleksander Hoffman, [a,b] Maja Romanowska, [a] Mikolaj Zychowicz, [a,b] Sebastian Baś, [a] Jakub J. Zakrzewski [a] and Szymon Chorazy *[a]

Lanthanide(III) single-molecule magnets (SMMs) are a tool for the combination of molecular nanomagnetism with luminescent thermometry, opening the pathway not only for broadened multifunctionality but also for the optical self-monitoring of temperature in SMM-based systems. Usually, this goal is realized by exploring the intrinsic properties of a single lanthanide (Ln) ion. We present an innovative strategy based on embedding magnetically anisotropic Ln(III) centers into a red-emissive coordination system based on Eu(III) complexes of a nonmagnetic ground state. This concept is presented for novel cyanido-bridged chains, $\{[Ln^{III}(dppmO_2)_3][Ag^{I}(CN)_2]\}[OTf]_2$ (Ln = Eu, **EuAg**; Ln = Er, **ErAg**; Ln = Yb, **YbAg**; Ln = $Er_{0.05}Eu_{0.95}$, **Er@EuAg**; Ln = $Yb_{0.04}Eu_{0.96}$, **Yb@EuAg**; $dppmO_2$ = bis(diphenylphosphino)methane dioxide; OTf = trifluoromethanesulfonate). The Ln(III) coordination sphere, consisting of O,O-bidentate $dppmO_2$ ligands occupying the equatorial positions and two axially aligned cyanido bridges, generates the distinct SMM characteristics of Er(III)/Yb(III) centers. Alternatively, the strong photoluminescence of Eu(III) in **EuAg** exhibits pronounced thermal variation of the excitation spectrum, which is employed for ratiometric optical thermometry, revealing a relative thermal sensitivity (S_r) of up to 2.1% K^{-1} at 55 K and a good thermometric response below 110 K. The incorporation of Er(III)/Yb(III) centers into the Eu(III)-based framework leads to heterotrimetallic **Er@EuAg** and **Yb@EuAg** systems, which link the SMM features with luminescent thermometry. Both physical properties are enhanced upon mixing of the Ln(III) centers, as depicted by the slow-down of magnetic relaxation, especially for Er(III), due to the Eu(III)-induced weakening of the quantum tunneling of magnetization, which is accompanied by the improved thermometric response, including an increase in the maximal S_r to 3.3% K^{-1} and broadening of its operating range to 150 K, due to the structural distortion induced by Er(III)/Yb(III) centers.

Received 5th October 2025,
Accepted 10th February 2026

DOI: 10.1039/d5qi02034d

rsc.li/frontiers-inorganic

Introduction

Driven by the demand for rapid miniaturization and increased efficiency of modern technologies based on new generations of optical, electronic, and magnetic devices, scientists have been motivated to search for multifunctional materials that can exhibit multiple physical functionalities in a single homogeneous phase.[1–10] The set of physical properties introduced can co-exist, such as in the materials linking photoluminescence, magnetism, electrical properties, or chirality.[11–17] They can also interact, leading to the great impact of one property on another, or even to new physical cross-effects, as exemplified by magneto-chiral dichroism (MChD) and circularly polarized luminescence (CPL).[18–23]

In the search for novel functional materials, especially those designed to achieve high-density data storage systems, the field of molecular nanomagnets emerged, offering magnetic phenomena induced at the molecular scale of matter.[24–30] Among them, lanthanide-based single-molecule magnets (SMMs) exhibit strong magnetic anisotropy, which is governed by the large spin–orbit coupling appearing along with the proper crystal field strength and symmetry.[31–37] Some lanthanide (Ln) SMMs were reported to simultaneously reveal various optical properties,[14–16] including photoluminescence (PL) originating from the f–f electronic transitions of 4f metal complexes.[38–40] This not only opens a pathway for bifunctional magneto-luminescent molecule-based materials but also enables the study of magneto-optical correlations, giving details about energy levels crucial for the SMM behavior.[41–45]

[a]*Faculty of Chemistry, Jagiellonian University, Gronostajowa 2, 30-387 Krakow, Poland. E-mail: simon.chorazy@uj.edu.pl*
[b]*Doctoral School of Exact and Natural Sciences, Jagiellonian University, Lojasiewicza 11, 30-348 Krakow, Poland*

Luminescent Ln-SMMs were also tested as candidates for the optical sensing of magnetic fields and, alternatively, the magnetic switching of PL.[46,47] Moreover, SMMs based on Ln(III) complexes are widely studied from the perspective of optical thermometry, as such a combination of properties can offer a strategy for an SMM-based device with the ability to self-monitor its temperature by an optical signal.[46] Several ways were applied for remote temperature detection in SMM-based molecular systems, including variation of the PL characteristics,[45–51] luminescence re-absorption,[52] or magnetic circular dichroism,[20] all related to the electronic transitions of 4f metal ions. Alternatively, it was shown that optical thermometry, including the most reliable ratiometric approach, could be generated for materials bearing Ln-SMMs but using the attached metalloligand as a source of a thermometric response.[53] This showed that there was the possibility of constructing advanced magneto-luminescent systems where molecular optical thermometers would be separated from the magnetic lanthanide center, ensuring the lack of any interfering effects from the thermometric read-out on the SMM performance; however, that work provided only a pathway for rather moderate optical thermometry relying on the broadband emission of the dicyanidoplatinate(II) metalloligand. Thus, the conclusion regarding the optimization of this approach for SMM-based optical thermometers was drawn.[53] It should also be noted that recently, a few other promising perspectives related to the integration of SMM behavior with optical thermometry were demonstrated. This includes the ability of dual synchronous luminescence sensing of temperature and magnetic field,[47] as well as the combination of magnetic and optical signals in achieving the extremely high sensitivity of temperature detection,[51] overcoming the limits inherently assigned to Boltzmann-type optical thermometers.[54] Moreover, very recent reports proved the great potential of the application of luminescent metal complexes, especially lanthanide(III)-based ones, in the construction of multi-readout molecular logic devices. This concept was realized by exploring the optical responsivity of these complexes to external stimuli, including the responsivity to magnetic fields, electromagnetic radiation, pH, temperature, and others.[55–57] In a broader research context, lanthanide(III)-based molecular systems are recognized as a source of impressive multifunctionality, which includes remarkable examples such as chiral magnetic materials with strong magneto-chiral dichroism being applied for the optical readout of SMM-based hysteresis loops,[58,59] the incorporation of luminescent lanthanide SMMs into an ionic framework that exhibits high proton conductivity and optical thermometry,[49] as well as magnetic complexes or clusters showing switchable magnetic circular dichroism (MCD).[60,61]

In this regard, aiming at a novel strategy for SMM-based optical thermometers, we decided to introduce magnetically anisotropic Ln(III) ions, considering typical best-performing SMM candidates such as Dy(III), Tb(III), Er(III), or Yb(III) centers,[62–66] into a strongly luminescent molecule-based matrix based on Eu(III) centers that revealed the nonmagnetic ground $^7F_0$ multiplet but strong red PL.[67–69] Due to showing only residual paramagnetism related to the thermally populated low-lying magnetic $^7F_1$ excited state, Eu(III) centers can be treated as diamagnetic at cryogenic temperatures, where the SMM behavior operates. Therefore, they are expected to serve as diamagnetic linkers contributing to the better isolation of magnetic Ln(III) centers in the crystal lattice; this is known to help optimize their SMM performance.[70] Moreover, the Eu(III) complexes offer strong red PL, which can be a source of luminescent thermometry even using this lanthanide ion exclusively, even though most related reports deal with their combination with other 4f metal ions, such as Tb(III).[71–74] To achieve an appropriate molecular platform to examine our concept of linking magnetically anisotropic Ln(III) centers with thermometry-inducing Eu(III) centers, we decided to employ an approach relying on linking lanthanide centers with cyanido metal complexes, which was shown to be an effective strategy for obtaining luminescent Ln-SMMs with tunable optical and magnetic characteristics, as well as the conjunction of molecular nanomagnetism with luminescent thermometry.[15,49,50,52,53,75] We selected dicyanidoargentate(I) ions, $[Ag^I(CN)_2]^-$, which could contribute to the stability of the framework as well as to tuning of the coordination sphere of Ln(III) centers for better SMM features, enhancing the latter by also serving as diamagnetic linkers that help with better magnetic isolation of Ln(III) centers.[76,77] They enable strong visible PL from Eu(III) centers due to the lack of absorption bands in the visible or NIR ranges, even offering a route to Eu-PL sensitization in the case of argentophilic stacks.[78,79] To generate Eu(III)-based optical thermometry based on visible PL, as the source of SMM behavior, we decided to work on Er(III) and Yb(III) centers, which, within typical down-shifting emission, are not PL-active in the visible range.[80–82] This selection demands an appropriate choice of supporting organic ligands that can provide negatively charged donor atoms to the equatorial positions of the coordination spheres of 4f metal ions. This was shown to be the best strategy for the stabilization of the favorable ground level of the highest m_J number for the Er(III) and Yb(III) SMMs of the prolate-type of electron density for the ground state.[31,83,84] Therefore, we decided to employ O,O-bidentate bis(diphenylphosphino)methane dioxide ligands ($dppmO_2$), belonging to the class of bis(phosphino) dioxide ligands that were reported to induce SMM behavior for prolate-type Ln(III) magnetic centers.[85,86] This type of ligand also possesses light absorption bands located in the high-energy UV range, which enables the exploration of Eu(III) PL in the visible range, with an eventual energy transfer pathway sensitizing this emission. As a result of combining a set of three types of molecular building blocks, namely, Ln(III) centers, $[Ag^I(CN)_2]^-$ ions, and $dppmO_2$ ligands, we report a series of heterometallic d–f cyanido-bridged coordination polymers with the general formula $\{[Ln^{III}(dppmO_2)_3][Ag^I(CN)_2]\}[OTf]_2$ (Ln = Eu, **EuAg**; Ln = Er, **ErAg**; Ln = Yb, **YbAg**; OTf^- stands for triflate ion, *i.e.*, trifluoromethanesulfonate ion), along with their mixed-Ln(III) analogs $\{[Eu^{III}_{0.95}Er^{III}_{0.05}(dppmO_2)_3][Ag^I(CN)_2]\}[OTf]_2$ (**Er@EuAg**) and $\{[Eu^{III}_{0.96}Yb^{III}_{0.04}(dppmO_2)_3][Ag^I(CN)_2]\}[OTf]_2$ (**Yb@Eu Ag**). **EuAg** exhibits ratiometric optical thermometry, relying on the

excitation spectrum for Eu(III) PL, while **ErAg** and **YbAg** analogs show SMM characteristics. More importantly, the mixed-Ln compounds exhibit the combination of Eu(III)-based optical thermometry and Er(III)/Yb(III)-based SMM features; both properties are enhanced upon the formation of heterotrimetallic systems. These effects were discussed based on X-ray diffraction, magnetic, and optical studies, which were supported by *ab initio* calculations employed to discuss both the luminescent and magnetic properties of the materials obtained.

Results and discussion

Structural characterization

Crystalline samples of **EuAg**, **ErAg**, and **YbAg**, and the analogous Eu(III) compounds containing a small amount of Er(III) and Yb(III) centers, *i.e.*, **Er@EuAg** and **Yb@EuAg**, respectively, were obtained through the self-assembly of the respective $Ln^{III}(OTf)_3$ salts, or suitable mixtures, with the $dppmO_2$ ligand and $K[Ag^{I}(CN)_2]$ inorganic precursor in the methanol/acetonitrile solutions. To obtain well-shaped crystals of these compounds, the abovementioned solutions containing the precursor mixtures were layered with diethyl ether, which induced crystallization (see Experimental section in the SI). Under such synthesis conditions, the series of five isostructural compounds with the general formula $\{[Ln^{III}(dppmO_2)_3][Ag^{I}(CN)_2]\}[OTf]_2$ (Ln = Eu, **EuAg**; Ln = Er, **ErAg**; Ln = Yb, **YbAg**; Ln = $Er_{0.05}Eu_{0.95}$, **Er@EuAg**; Ln = $Yb_{0.04}Eu_{0.96}$, **Yb@EuAg**; $dppmO_2$ = bis(diphenylphosphino)methane dioxide; OTf = trifluoromethanesulfonate) was obtained. The crystals for all these materials were suitable for single-crystal X-ray diffraction, which led to detailed insights into their crystal structures (Fig. 1 and S3–S7, Tables S1–S8). The phase purity and identity of all bulk samples of the compounds reported with their structural models were confirmed by powder X-ray diffraction (P-XRD) and supported further by additional physicochemical characterization using CHNS elemental analysis, IR absorption spectroscopy, and thermogravimetric (TG) analysis (see Experimental section and Fig. S1, S2, and S8). The metal composition of the mixed-lanthanide compounds, *i.e.*, **Er@EuAg** and **Yb@EuAg**, was determined using SEM-EDX analysis (Fig. S9, S10 and Tables S9 and S10).

For the whole series of five reported materials, the crystal structures consist of cationic coordination chains that are formed by eight-coordinated lanthanide(III) complexes, involving three neutral O,O-bidentate $dppmO_2$ ligands, which are further connected from two sides by $[Ag^{I}(CN)_2]^-$ anions, forming Ln(III)–NC–Ag(I) molecular bridges (Fig. 1). The resulting positive charge of the cyanido-bridged chains, which appears due to the 1 : 1 ratio of Ln(III) and Ag(I) centers, is counter-balanced by two OTf^- ions per formula unit, *i.e.*, the $\{Ln^{III}Ag^{I}\}$ pair. As determined by SC-XRD analysis, each compound contains one-half of a methanol molecule of crystallization per formula unit, which is removed upon drying in the air. This leads to the solvent-free composition for air-stable

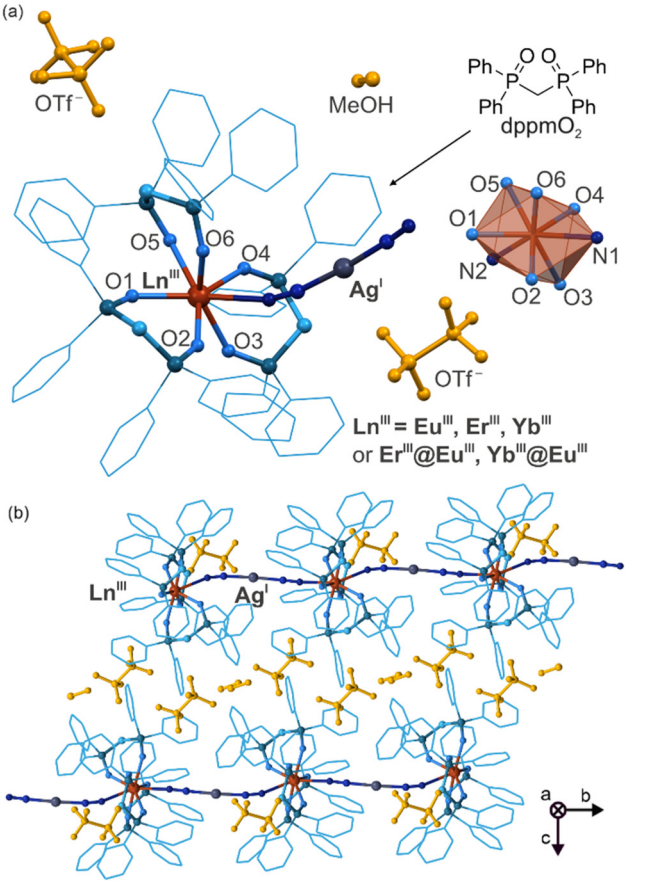

Fig. 1 Visualization of the crystal structure of the **EuAg**, **ErAg**, **YbAg**, **Er@EuAg**, and **Yb@EuAg** series (*i.e.*, Ln^{III}–Ag^{I} coordination polymers obtained with various Ln^{III} centers, as indicated), based on the structural model for **YbAg**, determined at 100(2) K, including insights into the molecular building unit, consisting of the Ln^{III} complex and $[Ag^{I}(CN)_2]^-$ anion, two triflate anions and a methanol molecule of crystallization with half occupancy, along with a detailed view of the first Ln^{III} coordination sphere (a) and the arrangement of coordination chains within the supramolecular network (b). In part (a), the chemical structure of the organic $dppmO_2$ ligand employed was added (Ph = phenyl).

samples, which, however, does not affect the crystal structure as proved by the P-XRD data (see Experimental section and Fig. S8 in the SI). The geometry of the lanthanide(III) $\{Ln^{III}O_6N_2\}$ coordination sphere within the whole series of compounds is a distorted dodecahedron (TDD-8), with the related CShM (continuous shape measures) parameters varying in the rather narrow range of 0.399–0.469, depending on the material, while bridging $[Ag^{I}(CN)_2]^-$ ions adopt a nearly linear geometry (Tables S7 and S8). Depending on the lanthanides included, the Ln–O and Ln–N distances vary subtly in the 2.247–2.442 Å and 2.438–2.593 Å ranges, respectively (Tables S2–S6). Noticeably longer Ln–O distances are observed for the Eu(III)-containing compounds, in particular **EuAg**, as expected due to their larger ionic radius in comparison to Er(III) and Yb(III) centers of a smaller and similar size. In all compounds, the Ln–O distances, related to the coordination of $dppmO_2$ ligands, are shorter than the Ln–N distances, related

to the cyanido ligands. Moreover, the cyanido ligands are arranged on the opposite sides of the complex. Thus, they can be considered as axial ligands, while three $dppmO_2$ ligands block the equatorial positions of the Ln(III) coordination spheres. Such an arrangement of ligands is known to be favorable for the SMM properties of Er(III) and Yb(III), showing the prolate type of electron density for the highest m_J levels of ground multiplet, especially since the equatorial positions are occupied by O-atoms of dioxide-type ligands bearing partial negative charges.[31] This promising structural prerequisite for the SMM features was examined by magnetic studies (see below). The three $dppmO_2$ ligands are not aligned perfectly in the equatorial plane due to the steric effects of large organic groups and the repulsion between O-atoms. As a result, they occupy six different positions of the dodecahedral coordination spheres, which are, however, elongated due to the two oppositely aligned N-atoms of the cyanido bridges. The latter are responsible for the overall formation of almost linear heterometallic chains. However, while the C–Ag–C angles are very close to the perfect value of 180°, the N–Ln–N angles significantly deviate from linearity, lying in the range of 144–146° (Tables S2–S6). This induces noticeable bending of the chains in the respective parts related to the Ln(III) complexes.

Experimental and theoretical studies of magnetic properties

Taking into account the coordination environment around the Er(III) and Yb(III) centers with three $dppmO_2$ ligands arranged in the equatorial positions and two cyanido ligands occupying the axial positions at distinctly longer distances (Tables S2–S6), which was promising for the appearance of slow magnetic relaxation effects for these lanthanide ions, we performed detailed direct-current (dc) and alternating-current (ac) magnetic studies on **ErAg** and **YbAg** (Fig. 2, 3, and S11–S17). Analogous studies have not been performed for **EuAg**, as it is known to reveal the nonmagnetic $^7F_0$ ground state with only weak temperature-induced paramagnetism related to the thermal population of a low-lying $^7F_1$ multiplet, which cannot lead to the slow magnetic relaxation phenomenon. We also performed ac and dc magnetic studies for compounds containing Er(III) and Yb(III) centers diluted with the previously mentioned Eu(III) complexes, *i.e.*, **Er@EuAg** and **Yb@EuAg** (Fig. 2, 3, and S18–S21), which could be treated as magnetically diluted samples due to the nearly diamagnetic signal from Eu(III) centers at low temperatures, in particular, in the temperature range below 10 K.[16]

The room-temperature $\chi_M T$ products of 11.27 and 2.48 $cm^3 mol^{-1} K$ for **ErAg** and **YbAg**, respectively, as well as the values of molar magnetization of 5.28 and 1.89μ_B, respectively, at 70 kOe at 1.8 K lie within the range typical of Er(III) and Yb(III) centers in coordination systems (Fig. S11–S13).[49,83,84] For both compounds, the $\chi_M T$ product gradually decreases upon cooling from 300 to 1.8 K; this can be mainly assigned to the cooling-induced depopulation of higher lying m_J states within the respective ground multiplets of Er(III)/Yb(III) centers separated by diamagnetic dicyanidoargentate(I) ions. To gain more precise insights into the magnetic properties of **ErAg** and **YbAg**, which were strongly related to the composition of the ground multiplets of Er(III) and Yb(III) complexes, respectively, relativistic SA-CASSCF (state-averaged complete active space self-consistent field) calculations were performed using the OpenMolcas (v23.06) program package.[87] They were further supported by simulations of the magnetic characteristics using the newly developed SlothPy software.[88] The results of this computational work are presented in Fig. 2c, 3c and S11–S13, S22–S26, as well as Tables S12–S15 (with the comment in the SI). The Er(III) centers in **ErAg** were found to be strongly anisotropic, revealing a high g_z value of 17.031 for the lowest-lying doublet of the ground multiplet. The magnetic axiality is significant, as also depicted by the dominance (89.4%) of the $|\pm 15/2\rangle$ m_J state for the previously mentioned lowest-lying doublet. The related easy axis of magnetization, represented by the g_z component of the pseudo-*g*-tensor, is situated close to the direction of two Ln–NC–Ag cyanido-based linkages (Fig. 2c and S24, S25). This confirms that the ground-state magnetic axiality is induced by three O,O-bidentate ligands that occupy the equatorial positions around the Er(III) center of the prolate-type shape of electron density for the highest possible, *i.e.*, $|\pm 15/2\rangle$, m_J state. This magnetic axiality is, however, not perfect, as proved by the g_x and g_y values for the ground doublet, which deviate significantly from 0, as well as by the non-negligible admixture of other-than-$|\pm 15/2\rangle$ m_J states in the composition of this ground doublet (Tables S12 and S13). The first excited doublet of the ground multiplet is placed 30.716 cm^{-1} above the ground one, and is highly mixed, which provides high values of related transverse components of g_x and g_y reaching 1.639 and 2.800, respectively. Using the SlothPy software, it was possible to simulate the broad range of magnetic characteristics for **ErAg** (Fig. S12, S13, S22, and S26). Among them, the computed $\chi_M T$ *versus* T plot was found to overlap with the experimental one for the T-range above 100 K, while a distinct discrepancy appeared at lower temperatures, *i.e.*, experimental values were lower than the simulated ones (Fig. S12). This indicates the presence of antiferromagnetic interactions between Er(III) centers despite their isolation in the crystal lattice by $[Ag^I(CN)_2]^-$ ions and $dppmO_2$ ligands. Their strength was determined by employing the Lines exchange model within the POLY_ANISO computational module using a coupling constant, J, of -0.2 cm^{-1}, which was estimated based on the fitting procedure of the experimental dc magnetic data. With the abovementioned J value, confirming non-negligible antiferromagnetic interactions operating in **ErAg**, it was possible to reproduce not only the $\chi_M T$ *versus* T plot well but also T-variable $M(H)$ dependences (Fig. S13). Such a situation does not happen in the case of Yb(III) centers in **YbAg**, for which both experimental $\chi_M T(T)$ and $M(H)$ plots are well reproduced by the ones simulated from the characteristics of the *ab initio*-calculated ground multiplet of Yb(III) (Fig. S11 and S13). This indicates the lack of noticeable magnetic interactions between the Yb(III) centers, for which magnetic isolation by other molecular components was found to be sufficient. On the other hand, magnetic anisotropy seems to be weakened for Yb(III) centers in **YbAg** in comparison to the

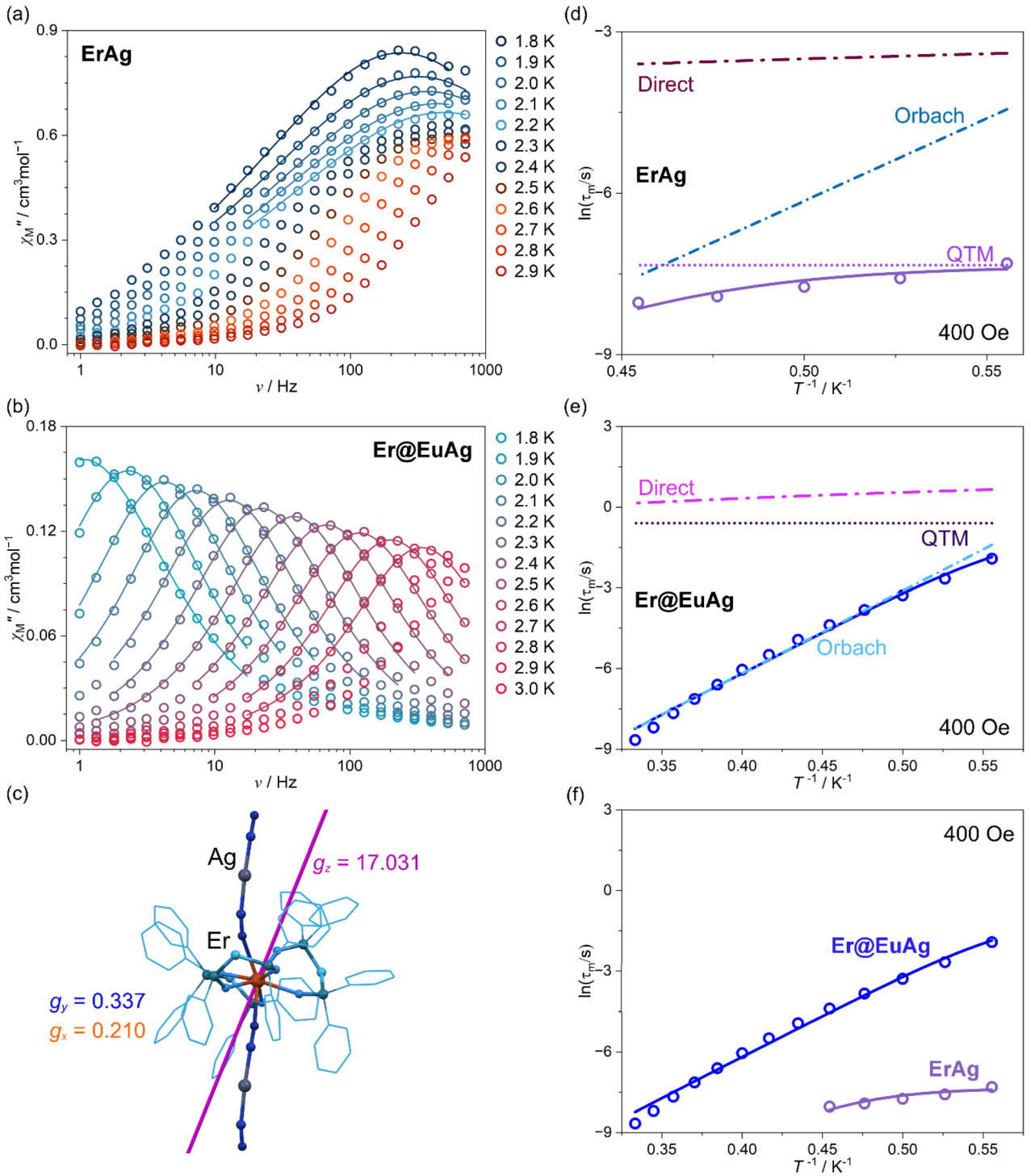

Fig. 2 Alternating-current (ac) magnetic characteristics of **ErAg** and **Er@EuAg**, including the frequency dependencies of the out-of-phase magnetic susceptibility, $\chi''_M(\nu)$, of **ErAg** (a) and **Er@EuAg** (b), at the temperatures indicated under a dc field of 400 Oe, and the temperature-dependencies of the resulting magnetic relaxation time, τ_m, for **ErAg** (d), **Er@EuAg** (e), and their comparison (f), and the alignment of the *ab initio*-calculated magnetic easy axis for the Er(III) centers in **ErAg** with the values of calculated pseudo-*g*-tensor components indicated (c). In (a and b), the best-fit curves to the generalized Debye model (eqn (1)) are shown as solid lines, while empty circles represent experimental data. In (d and e), the contributions of the relaxation processes indicated (direct, Orbach, QTM) to the overall relaxation time are depicted by dashed colored lines, while the solid lines (also in part (f)) represent the best-fit curves for their combined contributions (eqn (2) and Table 1). For the whole set of ac magnetic characteristics, please see Fig. S14, S15, S18, and S19.

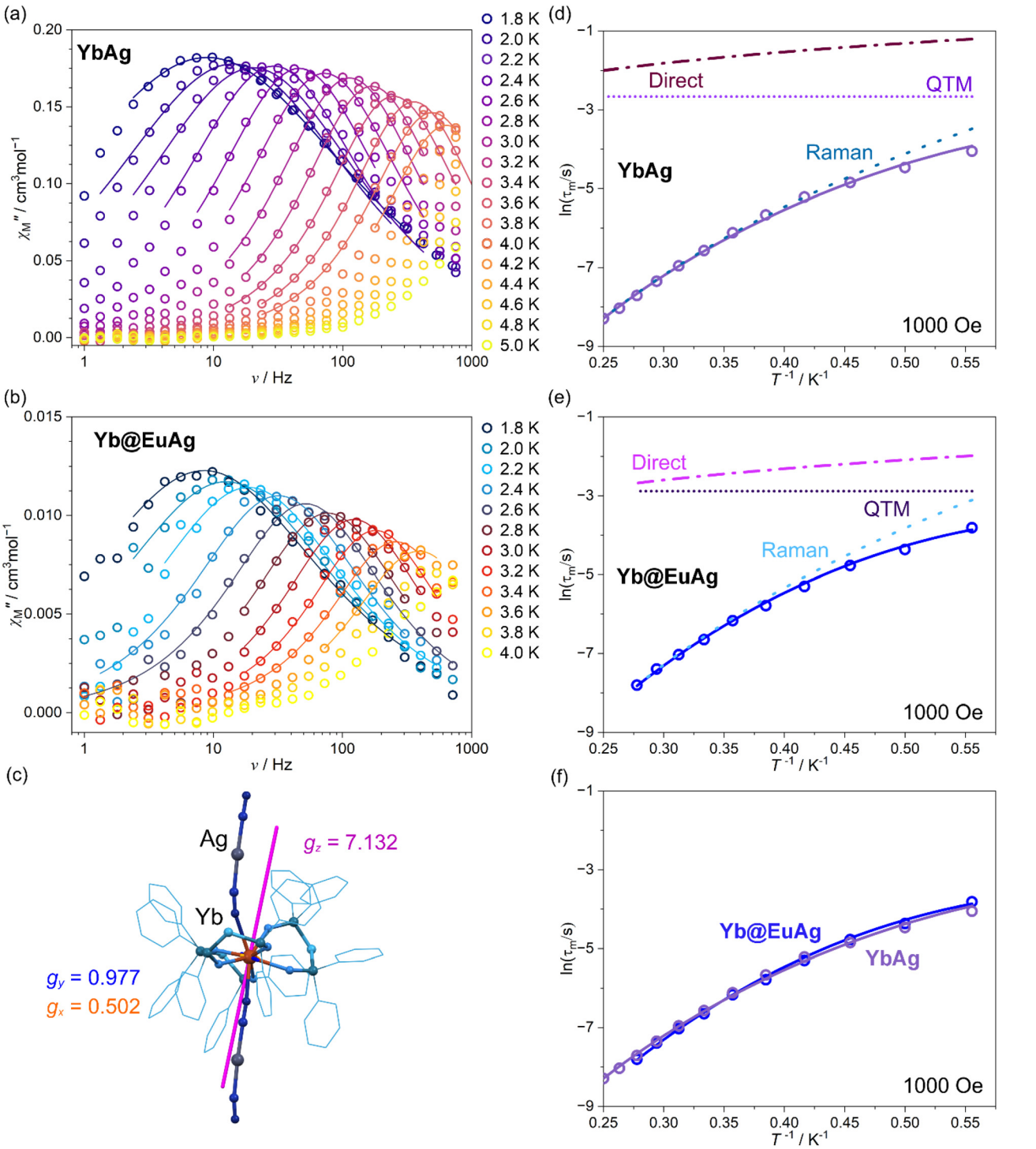

Fig. 3 Alternating-current (ac) magnetic characteristics of **YbAg** and **Yb@EuAg**, including the frequency dependencies of the out-of-phase magnetic susceptibility, $\chi_M''(\nu)$, of **YbAg** (a) and **Yb@EuAg** (b), at the temperatures indicated under a dc field of 1000 Oe, and the temperature-dependencies of the resulting magnetic relaxation time, τ_m, for **YbAg** (d), **Yb@EuAg** (e), and their comparison (f), and the alignment of the *ab initio*-calculated magnetic easy axis for the Yb(III) centers in **YbAg** with the values of calculated pseudo-*g*-tensor components indicated (c). In (a and b), the best-fit curves to the generalized Debye model (eqn (1)) are shown as solid lines, while empty circles represent experimental data. In (d and e), the contributions of the relaxation processes indicated (direct, Raman, QTM) to the overall relaxation time are depicted by dashed colored lines, while the solid lines (also in part (f)) represent best-fit curves for their combined contributions (eqn (2) and Table 1). For the whole set of ac magnetic characteristics, please see Fig. S16, S17, S20, and S21.

analogous features of Er(III) complexes in **ErAg**. The easy-axis type of magnetic anisotropy is similar in both compounds, as visualized by the main magnetic axis, which, in **YbAg**, is also represented by the dominant g_z value and placed close to the direction of Ln–NC–Ag molecular bridges (Fig. 3c). This is not surprising as both Er(III) and Yb(III) centers reveal prolate-type electron density for the highest possible m_J level; thus, the $dppmO_2$ ligands induce a similar easy-axis-type anisotropy for both cases. However, the corresponding g_z value of 7.132 in **YbAg**, representing the lowest-lying doublet of the ground multiplet, is much lower than that for **ErAg**; this is mainly related to the lower value of the highest possible m_J level of $|\pm 7/2\rangle$. The latter state dominates the composition of the ground Kramers doublet (85.5%, Table S15); however, admixtures of the other m_J states are significant, *i.e.*, 7.7% of $|\pm 3/2\rangle$. This leads to significant values of the ground-state g_x and g_y values of 0.502 and 0.977, which are much higher than those of the ground state of **ErAg**. The first excited doublet lies very high in energy, *i.e.*, 200.46 cm^{-1} above the ground one. Similarly to **ErAg**, it is highly mixed with a particularly large g_y value of 1.345 (Table S14). From these computational results, it can be stated that significant axial magnetic anisotropy, suitable for the SMM effect, is induced in both **ErAg** and **YbAg**. To confirm this, ac magnetic measurements were performed as a function of temperature and magnetic field, and related results are gathered in Fig. 2, 3, and S14–S21, as well as Tables 1 and S11.

The samples of **ErAg** and **YbAg**, as well as **Er@EuAg** and **Yb@EuAg**, do not demonstrate a noticeable signal of the out-of-phase magnetic susceptibility, χ''_M, in zero dc field, indicating the lack of slow magnetic relaxation without the quenching of zero-field quantum tunneling of magnetization (QTM) by an external magnetic field. This agrees with the results of *ab initio* calculations that indicated the significant values of transverse components of the ground-state pseudo-*g*-tensors (Fig. 2c and 3c). However, even under a small applied external dc magnetic field, all compounds listed reveal the presence of maxima at 1.8 K in the $\chi''_M(\nu)$ dependencies. Based on the dc-magnetic-field variable $\chi''_M(\nu)$ curves (Fig. S14, S16, S18, and S20), the optimal dc field was estimated to be *ca.* 400 Oe for **ErAg** and **Er@EuAg**, and *ca.* 1 kOe for **YbAg** and **Yb@EuAg**. For the optimal dc field, the set of *T*-variable ac magnetic curves was collected, and distinct maxima on the $\chi''_M(\nu)$ plots were observed, indicating the appearance of field-induced SMM behavior. It happens within the accessible 1–1000 Hz frequency range, at 1.8–3.0 K for the Er(III)-containing compounds and 1.8–4.0 K for the Yb(III)-containing ones. The abovementioned $\chi''_M(\nu)$ curves, together with related $\chi'_M(\nu)$ and $\chi''_M(\chi'_M)$ plots, were fitted in the relACs software, using the generalized Debye model for a single magnetic relaxation process (eqn (1)).[88–90]

$$\chi(\omega) = \chi_\infty + \frac{\chi_0 - \chi_\infty}{1 + (i\omega\tau_M)^{1-\alpha}} \quad (1)$$

where $\chi(\omega)$ is a complex magnetic susceptibility containing real and imaginary parts, *i.e.*, $\chi = \chi' - i\chi''$ and $\omega = 2\pi\nu$; χ_0 is the isothermal susceptibility (for the limit of $\nu \to 0$), χ_∞ is the adiabatic susceptibility (for the limit of $\nu \to \infty$), τ_M is the magnetic relaxation time, and α is the parameter describing the distribution of relaxation times. The magnetic relaxation times, τ_M, which were extracted from the related best-fit curves (Fig. 2d, e, 3d, e, and S14–S21), were further analyzed within the global fit of the $\tau_M(T,H)$ dependence, implemented in relACs. Various combinations of possible magnetic relaxation processes were considered, which included QTM, direct, Orbach, and Raman relaxation pathways.[88–90] For Er(III)-containing **ErAg** and **Er@EuAg**, the $\tau_M(T,H)$ dependencies provided the most reasonable fits, taking into account three relaxation processes, as represented by eqn (2):

$$\tau_M^{-1} = \frac{a}{(1 + bH^2)} + AH^m T + \tau_0 \exp\left(\frac{-\Delta E}{k_B T}\right) \quad (2)$$

where the first term corresponds to the quantum tunneling of magnetization (QTM), depicted by two parameters (a and b), the second represents the direct process, while the third parameterizes the Orbach relaxation pathway, for which ΔE could be extracted from *ab initio* calculations as the energy position of the first excited ground doublet, revealing a highly mixed m_J composition (see above). The resulting best-fit parameters and related visualization of contributions from all relaxation processes for **ErAg** (Fig. 2d; Tables 1 and S11) indicate a predominant role of the QTM process, which is not fully quenched by the external magnetic field. Upon increasing the external dc field, the QTM is gradually quenched; however, the direct process starts to govern the overall relaxation. Therefore, even

Table 1 Summary of best-fit slow magnetic relaxation parameters for **ErAg**, **YbAg**, **Er@EuAg**, and **Yb@EuAg** obtained within the three-dimensional simultaneous fitting of the field dependence (T = 1.8 K) and temperature dependence (optimal dc field indicated in Fig. 2 and 3) of respective magnetic relaxation times

Compound	**ErAg** (Fig. 2a, d, f and S14, S15; eqn (2))	**Er@EuAg** (Fig. 2b, e, f and S18, S19; eqn (2))	**YbAg** (Fig. 3a, d, f and S16, S17; eqn (3))	**Yb@EuAg** (Fig. 3b, e, f and S20, S21; eqn (3))
$A/s^{-1}\ K^{-1}\ Oe^{-m}$	$8.3(6) \times 10^{-10}$	$8.9(3) \times 10^{-10}$	$3.6(2) \times 10^{-10}$	$1.7(2) \times 10^{-9}$
m	3.96(3)	3.27(5)	3.24(1)	2.79(1)
a/s^{-1}	3468(731)	5.89(3)	171(52)	$4.43(2) \times 10^{9}$
b/Oe^{-2}	$7.8(8) \times 10^{-6}$	$1.4(9) \times 10^{-5}$	$1.1(6) \times 10^{-5}$	247(31)
$B/s^{-1}\ K^{-n}$	0 (fixed)	0 (fixed)	0.94(24)	0.42(12)
n	0 (fixed)	0 (fixed)	6.02(23)	6.78(27)
τ_0/s	$2.18(3) \times 10^{-9}$	$1.05(6) \times 10^{-8}$	0 (fixed)	0 (fixed)
$\Delta E/cm^{-1}$	30.716 (*ab initio*)	30.716 (*ab initio*)	0 (fixed)	0 (fixed)

for the optimal dc field, for **ErAg**, the $\chi''_M(\nu)$ maxima are visible only in the very limited *T*-range below 3 K. The Orbach relaxation occurs for **ErAg** but is less pronounced than QTM, except for the highest accessible temperatures close to 3 K. More importantly, upon dilution of Er(III) centers in the Eu(III)-based matrix, *i.e.*, for the sample of **Er@EuAg**, a distinct shift of magnetic relaxation times to the lower frequency region is observed (Fig. 2b). This indicates the distinct improvement of SMM features upon magnetic dilution from **ErAg** to **Er@EuAg**. A thorough analysis of the ac data for **Er@EuAg** (Fig. 2 and S18, S19) indicates that magnetic dilution mainly affects the QTM, which is drastically slowed down. As a result, magnetic relaxation starts to be governed by the Orbach process related to the two-phonon-assisted transition through the first excited Kramers doublet, as the related calculated energy of this state could be successfully used in the fitting procedure as the Orbach energy barrier. Thus, it seems that magnetic dilution with Eu(III) centers ensures the efficient magnetic isolation of Er(III) centers, cancelling out the QTM effect, which is promoted for the undiluted analog bearing residual antiferromagnetic interactions (as determined and discussed above). The Orbach process, which becomes the limiting one in **Er@EuAg**, remains almost identical to that found for the undiluted compound, which is not unexpected, as the Er(III) coordination sphere is only subtly altered by dilution with Eu (III) centers.

It should be noted that, in the fitting procedure for the $\tau_M(T,H)$ dependencies for **ErAg** and **Er@EuAg**, we also tested various alternative approaches, including fitting of the energy barrier of an Orbach relaxation instead of its fixing from the results of the *ab initio* calculations, as well as exchange of the Orbach relaxation for the Raman one, or even the use of four co-existing relaxation processes (Raman, direct, QTM, and Orbach) instead of the three processes presented. The results for some of the alternative fitting procedures of the above-mentioned types are shown in the SI (Fig. S44, S45 and Table S29); however, they all produce less reliable results than those shown above, and also provide a less consistent comparison between **ErAg** and its magnetically diluted form of **Er@EuAg** (see the comment to Fig. S44 and S45, and Table S29 in the SI for a broader discussion).

For the Yb(III)-based systems, **YbAg** and **Yb@EuAg**, the magnetic relaxation times, considered as a function of magnetic field (H) and temperature (T), were successfully fitted by taking into account three relaxation processes, as given by eqn (3):

$$\tau_M^{-1} = \frac{a}{(1+bH^2)} + AH^mT + BT^n \quad (3)$$

with the three components corresponding to the QTM, direct, and Raman relaxation processes (Fig. 3 and S16, S17, S20, S21, as well as Tables 1 and S11). In this case, the Orbach process was excluded due to a large discrepancy between the energy barriers extracted using *ab initio* calculations (*i.e.*, the energy position of the first excited doublet, Table S14) and the experimental energy barrier suggested by preliminary fits employing the Arrhenius-type dependence of the relaxation time. The best-fit parameters and their representation, given by contributions from each relaxation process included (Fig. 3d), for **YbAg**, indicated the main role of the Raman process in the SMM behavior, with the weaker contributions originating from the QTM and direct processes. This scenario is the usual one for the case of Yb(III) SMMs.[49,84] The magnetic dilution of **Yb@EuAg** with **YbAg** was found to only weakly affect, *i.e.*, slightly improve, the SMM features. Only subtle differences, *e.g.*, in the non-negligible increase of the power n for the Raman relaxation and the concomitant decrease in the related B parameter, are observed upon the dilution of Yb(III) centers with Eu(III) ones. This effect can be correlated with changes in the phonon mode schemes upon the partial replacement of smaller Yb(III) centers with larger Eu(III) complexes. In contrast, the QTM was found to be almost insensitive to magnetic dilution, which could have been expected as the QTM-enhancing Yb–Yb magnetic interactions were not detected, even for the undiluted material, **YbAg** (see above).

From the above discussion, it is seen that the Eu(III)-based magnetic dilution effect improves the SMM features, but mainly in the case of **Er@EuAg** due to the cancelling out of crucial Er–Er magnetic interactions, while the Eu(III) centers have only a minor impact on the magnetic features of Yb(III) centers in **Yb@EuAg**. It should be remembered that Eu(III) centers reveal a nonmagnetic ground state; however, even at low temperature, residual paramagnetism remains due to the low-lying excited states with a paramagnetic characteristic. Therefore, to further examine if the Eu(III)-based matrix provides efficient magnetic dilution of embedded Er(III) and Yb(III) centers, analogous compounds employing perfectly diamagnetic Y(III) centers instead of Eu(III) are used. The resulting materials, abbreviated as **Er@YAg** and **Yb@YAg** for Y(III)-diluted Er(III) and Yb(III), respectively, were characterized by P-XRD patterns and SEM-EDX metal analysis (Fig. S48–S50 and Tables S30, S31, with the comment in the SI). These studies proved that **Er@YAg** and **Yb@YAg** were isostructural to the reported series of compounds and contained a small amount of magnetic lanthanide centers diluted with Y(III), *i.e.*, the Ln-metal compositions of $Y_{0.94}Er_{0.06}$ (**Er@YAg**) and $Y_{0.95}Yb_{0.05}$ (**Yb@YAg**) were found. Then, the ac magnetic properties of **Er@YAg** and **Yb@YAg** were investigated under variable magnetic fields and temperatures (Fig. S51–S55 and Table S32). These measurements indicate that **Er@YAg** and **Yb@YAg** exhibit very similar field-induced slow magnetic relaxation effects to those detected in their Eu(III)-containing analogs **Er@EuAg** and **Yb@EuAg**, respectively. Therefore, the related $\tau_M(T,H)$ dependencies for **Er@YAg** and **Yb@YAg** could be reliably fitted using identical sets of magnetic relaxation processes, *i.e.*, the combination of direct, QTM, and Orbach, for **Er@YAg** (the same as for **Er@EuAg**), while the combination of direct, QTM, and Raman was used for **Yb@YAg** (the same as for **Yb@EuAg**) (Fig. S55 and Table S32). Moreover, the *T*- and *H*-dependences of relaxation time for **Er@YAg**, and the resulting best-fit parameters describing individual relaxation processes, are almost identical to those found for **Er@EuAg**. This

includes the very similar contribution from the QTM effect, with even subtly better (*i.e.*, slower relaxation) quenching of the QTM for the Eu(III)-based dilution. This strongly indicates that the disruptive Er–Er interactions are fully cancelled out by the Eu(III) centers and their residual paramagnetism, which might remain even at low temperatures, does not contribute to the promotion of the QTM effect. In other words, these results confirm that, from the viewpoint of magnetic dilution, the Eu(III) centers work equally as well as the Y(III) ones for the obtained coordination systems. The situation seems to be different in the case of **Yb@YAg**, for which Y(III)-based dilution leads to the subtle enhancement of slow magnetic relaxation in comparison to Eu(III)-based dilution in **Yb@EuAg** (Fig. S55 and Table S32). However, this effect is mainly governed by the improved Raman relaxation pathway, which is not correlated with unquenched magnetic interactions but is usually directly related to the modulation of the phonon mode scheme assisting in this type of spin–lattice relaxation. Moreover, the dc magnetic data, combined with the results of *ab initio* calculations (see above), for undiluted **YbAg**, indicate the lack of Yb–Yb magnetic interactions in this compound; this agrees well with the very small change in the QTM effect upon Eu(III)-based dilution. Therefore, the improved SMM features upon Y(III)-based dilution should be ascribed to the variation of the phonon modes upon the usage of much lighter Y(III) centers rather than the heavier Eu(III) complexes as a matrix for magnetic dilution. In fact, the direct, QTM, and Raman relaxation processes are affected by Y(III)-based dilution, which suggests that changing the matrix to the Y(III)-containing one induces not only changes to the phonon modes but also some non-negligible changes to the metric and/or geometrical parameters of the coordination sphere of embedded magnetic Yb(III) complexes. However, taking into account the abovementioned identical results for Y(III)- and Eu(III)-based dilutions in the case of Er(III), and the proven negligibly small magnetic interactions between Yb(III) centers for undiluted **YbAg**, it can be stated that magnetic dilution by Eu(III) centers is also efficient (in the context of cancelling out the magnetic interaction) for Yb(III) centers, even though the Y(III) centers provide better SMM features thanks to the beneficial modulation of the other aspects, such as the phonon-assisted relaxation routes.

Experimental and theoretical studies of optical properties

Solid-state UV-vis absorption spectra were measured for the polycrystalline powder samples of all coordination systems obtained (Fig. S28). All of them exhibit strong absorption in the UV region, in the 200–290 nm range, which is attributed to the electronic transitions of $dppmO_2$ ligands and $[Ag^{I}(CN)_2]^-$ ions, through their $n \rightarrow \pi^*/\pi \rightarrow \pi^*$ and $^1\Sigma_{g+}$; $^1\Delta_{g+} \rightarrow {}^1\Pi_u$ electronic transitions, respectively.[76,77,91] The light absorption bands corresponding to the f–f electronic transitions, which could have been observed in particular for Er(III) centers, are not visible in the UV-vis range due to their Laporte forbidden characteristic, leading to their low relative intensities.[92]

Among the non-diluted compounds, under UV light excitation, only **EuAg** reveals photoluminescence (PL) related to the f–f electronic transitions of respective Ln(III) centers (Fig. S29).[92,93] This PL signal provides the red color of emission, which is typical of Eu(III)-containing materials. The analogous PL for Er(III) and Yb(III) centers should appear in the NIR range, but the related emission was not observed, even at 77 K, most probably due to the lack of a suitable sensitizer for this PL and the dominance of non-radiative relaxation pathways through the vibrational states, *e.g.*, of expanded organic groups. The emission spectrum for **EuAg** at 310 K contains well-defined emission bands, centered at *ca.* 580, 589, 613, 650, 700, and 747 nm, which can be associated with the set of $^5D_0 \rightarrow {}^7F_{0-5}$ electronic transitions (Fig. S27 and S29).[92,93] The obtained pattern comprises several emissive components for each band, which are associated with the m_J levels of each multiplet, apart from the unsplit ground $^7F_0$ state. To fully confirm the assignment of emission bands, the energy positions of related Eu(III)-centered f–f electronic transitions were calculated using the *ab initio* SA-CASSCF method, and an attempt to simulate the spectra was performed (Fig. S27 and Tables S16–S21, and the related comment on page S34 of the SI). With the support of the overall energy shift to the $^5D_0 \rightarrow {}^7F_0$ line, such a simulation reproduces experimental spectra at 10 K well and confirms the assignment of each of the observed bands to the Eu(III) f–f electronic transition. Within the experimental spectrum, the most intense maximum is located at *ca.* 613 nm, which corresponds to the $^5D_0 \rightarrow {}^7F_2$ electronic transition. Moreover, here the $^5D_0 \rightarrow {}^7F_4$ electronic transition, which is usually the one most affected by the crystal field and its geometry,[93] provides the second most intense band with the main maximum at *ca.* 700 nm. Its intensity is very similar to the peak related to the $^5D_0 \rightarrow {}^7F_2$ transition, which is not typical behavior, as usually this higher energy band dominates the emission spectrum of Eu(III) centers.[93] However, for a series of Eu(III)-based luminophores, including the metal complex-type ones, the intensity of the lower-energy bands corresponding to the $^5D_0 \rightarrow {}^7F_4$ electronic transition can be of similar intensity to the band related to the $^5D_0 \rightarrow {}^7F_2$ transition, or even stronger, for the cases of the D_{4d} symmetry of the Eu(III) centers (*e.g.*, a square antiprism), or lower symmetries that are distorted towards D_{4d} symmetry.[93] This agrees well with the results of the continuous shape measures analysis performed for the Eu(III) centers in **EuAg** (Table S7), which reveal that these complexes can be described as dodecahedral (D_{2d} symmetry) but deformed towards the square antiprism of the aforementioned D_{4d} symmetry. Upon changing the temperature, the emission pattern barely changes, while the overall emission intensity increases upon cooling, as expected for Ln(III)-based luminophores, where cooling usually limits non-radiative relaxation through the vibrational states or thermally activated energy back transfer processes (Fig. S29).[92,93]

To better discuss the electronic transitions and related molecular components responsible for the observed Eu(III) emission in **EuAg**, its excitation spectra were also collected

(Fig. S29). At 310 K, in the 290–470 nm range, several excitation peaks can be distinguished. They can be assigned to direct f–f excitation through the following set of f–f electronic transitions: $^7F_0 \rightarrow {}^5D_2$ at *ca.* 464 nm, $^7F_0 \rightarrow {}^5D_3$ (*ca.* 424 nm), $^7F_0 \rightarrow {}^5L_6$ (*ca.* 393 nm), $^7F_0 \rightarrow {}^5L_7$ (*ca.* 382 nm), $^7F_0 \rightarrow {}^5G_{3-6}$ (*ca.* 374 nm), $^7F_0 \rightarrow {}^5D_4$ (*ca.* 360 nm), and $^7F_0 \rightarrow {}^5H_{4-7}$ (*ca.* 316 nm).[93] The broad excitation bands that can be attributed to the electronic transitions of the organic $dppmO_2$ ligand are situated below *ca.* 300 nm, which indicates at least partial energy transfer to the Eu(III) centers. Upon lowering the temperature, the excitation related to the ligand narrows and increases in intensity. An additional excitation band emerges at *ca.* 316 nm, which can be associated with the $^7F_0 \rightarrow {}^5H_3$ electronic transition. The most intense direct excitation corresponds to the $^7F_0 \rightarrow {}^5L_6$ transition at *ca.* 393 nm. Most of the peaks related to the direct f–f excitation increase upon cooling; however, the increase is weaker than the ligand-based excitation. Moreover, some of the peaks, *e.g.*, those in the 380–390 nm range, undergo an intensity decrease upon cooling. This behavior is typical of excitation through the hot f–f electronic transitions from the $^7F_1$ multiplet, which becomes gradually depopulated upon lowering the temperature.[93] Thus, it is clearly seen that the excitation pattern of **EuAg** is strongly temperature-dependent. This is a prerequisite for the usage of this compound as a luminescent thermometer, as examined and discussed in the next section (see below).[94,95]

At 310 K, the emission spectrum for the mixed-lanthanide system, **Er@EuAg**, which was shown in the previous section to exhibit SMM features, is very similar to that observed for **EuAg**; thus, it can be analogously assigned to the Eu(III) f–f electronic transitions, as confirmed by the literature and *ab initio* calculations (Fig. 4a, b and S29). Similar to **EuAg**, the emission spectrum for **Er@EuAg** (and **Yb@EuAg**) contains the strongest band corresponding to the $^5D_0 \rightarrow {}^7F_2$ electronic transition; however, the lower-energy bands related to the $^5D_0 \rightarrow {}^7F_4$ transition are of very similar intensity. This can analogously be rationalized by the adopted Eu(III) coordination geometry close to the dodecahedral one but distinctly deformed towards the square antiprism of D_{4d} symmetry (Table S7), which is responsible for the unusual enhancement of the peaks related to the $^5D_0 \rightarrow {}^7F_4$ transition.[93] However, some noticeable changes in the intensity ratio between the emission bands corresponding to the $^5D_0 \rightarrow {}^7F_2$ and $^5D_0 \rightarrow {}^7F_4$ electronic transitions can be reported. They are assignable to the small distortion of the geometric parameters within the first coordination sphere of the Eu(III) centers that happens upon the incorporation of Er(III) complexes of smaller size (Tables S2, S3, and S5). A detailed analysis of related SC-XRD data reveals the shortening of the Ln–O distances (from 2.33–2.43 Å in **EuAg** to 2.25–2.38 Å in **Er@EuAg**). For the Yb(III)-doped system, **Yb@EuAg**, the analogous emission changes in comparison to those of **EuAg** are less pronounced (Fig. 4a and S29). This observation seems to be consistent with smaller changes in the Ln–O distances in the crystal structure of **Yb@EuAg**, which lie in the 2.32–2.44 Å range; thus, they are generally very

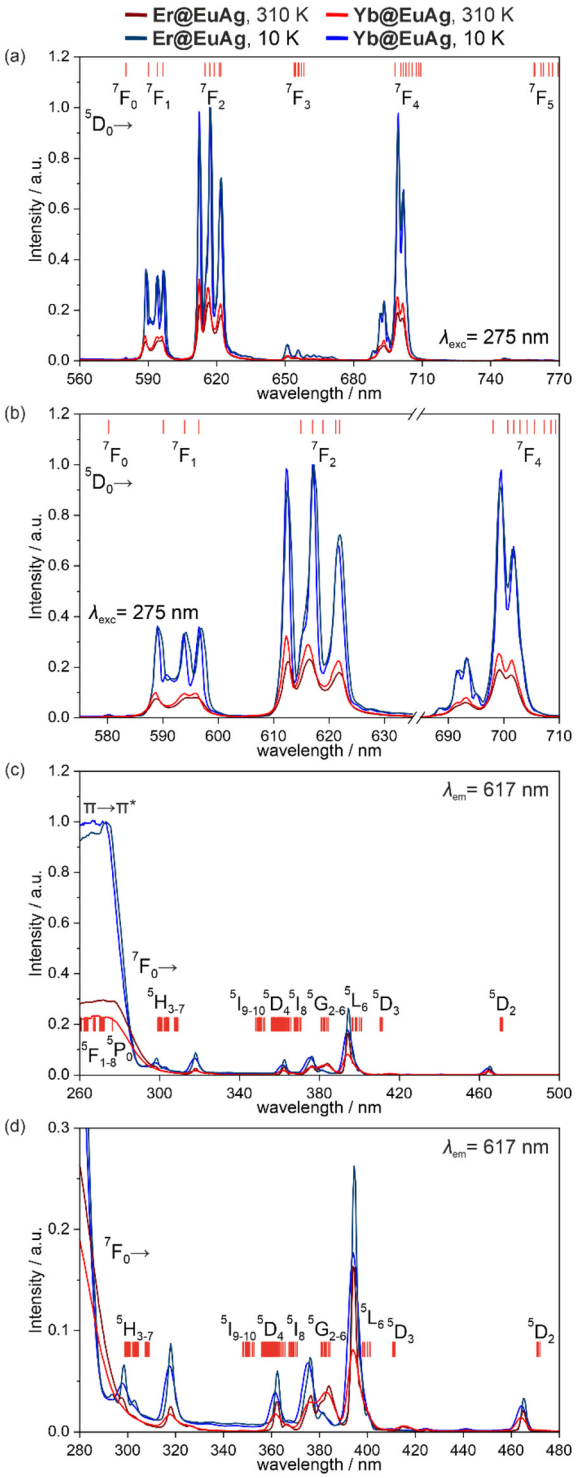

Fig. 4 Solid-state photoluminescent properties of **Er@EuAg** and **Yb@EuAg** at 310 K and 10 K, including emission spectra for the 275 nm excitation (a), and its enlargement over the $^5D_0 \rightarrow {}^7F_{0-2}$ and $^5D_0 \rightarrow {}^7F_4$ areas (b), and excitation spectra for the 617 nm emission (c), with an enlargement of the 280–480 nm range (d). The selected f–f electronic transitions of Eu(III) centers in **Er@EuAg** and **Yb@EuAg** are labelled in both parts of the figure; the π–π* electronic transitions with the organic ligand were indicated in part (b). At the top of the emission (a) and excitation spectra (b), the *ab initio* calculated energy positions of the Eu^{III} excited states are shown. They were calculated using the crystal structure of **EuAg** (see comment on Fig. S22–S27 and Tables S12–S21 in the SI).

similar, at least in the metric range, to **EuAg** (Tables S2, S4, and S6). On the other hand, temperature-induced changes in the emission spectra of **Er@EuAg** and **Yb@EuAg** are very similar.

The excitation spectra of **Er@EuAg** and **Yb@EuAg** at 310 K contain a broad, strong band assignable to the $\pi \rightarrow \pi^*$ electronic transition of the organic $dppmO_2$ ligand lying below 300 nm, as well as the series of sharp, weaker peaks in the 300–500 nm range, related to the well-defined f–f electronic transitions of the Eu(III) centers (Fig. 4c, d and S29).[93] Both of these groups of excitation peaks are situated in analogous wavelength positions to those found in **EuAg**; thus, their assignment to the characteristic electronic transition is similarly confirmed by previous reports and calculations performed (Fig. 4c and d). The differences between **Er@EuAg** and **Yb@EuAg** are only subtle. In particular, for **Yb@EuAg**, it seems that, at 310 K, the excitation band related to the $dppmO_2$ ligand is relatively weaker, suggesting a slightly weaker ligand-to-metal (*i.e.*, to-Eu) energy transfer (ET) process or the better efficiency of direct f–f excitation. The latter effect can be considered to be more probable, as the Er(III) centers reveal the number of excited states in the 300–500 nm range, which can be disturbing for the direct f–f excitation, while Yb(III) centers do not possess any excited states in this energy region. More importantly, upon cooling, the excitation bands related to the organic ligand, as well as the bands assigned to most of the direct f–f excitation routes, increase their intensity. The stronger cooling-induced enhancement of the intensity is observed for the ligand's bands, indicating the strongly *T*-dependent ET process, probably due to the thermally activated energy back transfer that often governs the thermal variation of the ligand sensitization of lanthanide PL.[93,94] Similarly to **EuAg**, only a few excitation peaks related to direct f–f excitation, *e.g.*, the band lying in the 380–390 nm range (Fig. 4b), reveal very different *T*-dependences, as they undergo an intensity decrease upon cooling (*i.e.*, the intensity increases upon heating). Thus, they can be assigned to the hot f–f electronic transitions from the lowest-lying excited $^7F_1$ multiplet.[93] The abovementioned band in the 380–390 nm range can then be ascribed to excitation through $^7F_1 \rightarrow {}^5G_{2-6}$ transitions. Based on these observations, **Er@EuAg** and **Yb@EuAg** could be postulated to be promising candidates for realizing optical thermometry utilizing excitation spectra (see the related studies below).[95]

To complete the basic photophysical characterization, the emission decay profiles were collected for Eu(III)-based PL for **EuAg**, **Er@EuAg**, and **Yb@EuAg**. They were analyzed using the mono-exponential decay function (Fig. S32–S43 and Tables S25–S27), which was consistent with the single crystallographic position of Eu(III) centers in the systems obtained. The resulting emission lifetimes, collected using the 275 nm through-ligand excitation and monitoring the 617 nm PL peak, change subtly upon doping **EuAg** with Er(III) and Yb(III). At 310 K, **EuAg** exhibits an emission lifetime of 2.534(4) ms, which increases upon cooling to 2.644(3) ms at 10 K. The insertion of Er(III) centers into **Er@EuAg** shifts the emission lifetimes to slightly lower values of 2.450(7) ms at 310 K and 2.544(3) ms at 10 K, while Yb(III) doping yields an increase in the emission lifetime to 2.591(5) ms at 310 K and 2.740(3) ms at 10 K. This non-trivial modulation of the emission lifetime by the Ln(III) dopants investigated can be rationalized by taking into account two effects. The first is that the insertion of Er(III) and Yb(III) centers into the framework leads to better separation of emissive Eu(III) complexes, at least partially limiting the unbeneficial cross-relaxation and energy transfer processes between neighboring Eu(III) centers. This contributes to the increase in the emission lifetime upon the addition of dopants. However, there is also the second concomitant effect related to the non-radiative relaxation of the Eu(III) emission through the excited states of the Ln(III) dopants if they are positioned in a similar energy range to that of the emissive state of Eu(III). This contributes to the decrease in the emission lifetime. **Yb@EuAg** can show the first beneficial effect, while the second one does not operate, as the Yb(III) centers reveal only a very low-lying excited state with an energy corresponding to the NIR range. As a result, the Yb(III) dopants induce the increase in the Eu(III) emission lifetime. In contrast, even though **Er@EuAg** can still reveal the first effect, it exhibits the second effect in a more pronounced way, having a series of excited states corresponding to the visible range of the spectrum. As a result, the overall shortening of the Eu(III) emission lifetime is observed upon the addition of Er(III) centers.

The emission color within the whole series of compounds remains constant at 310 K. The temperature change also has a negligible impact on the extracted CIE 1931 parameters, confirming red PL for the materials obtained (Fig. S31 and Table S24). The absolute quantum yields (QYs) of the solid-state samples at room temperature remain consistent across the three compounds mentioned, reaching 55.36% for **EuAg**, 54.48% for **Er@EuAg**, and 54.12% for **Yb@EuAg** (Table S28). These high values correspond not only to the relatively good sensitization of the Eu(III) PL by the $dppmO_2$ ligand but also to the efficient shielding of the emissive centers by these ligands and cyanido bridges from the environment, *e.g.*, solvent molecules of crystallization, which could have been the reason for emission quenching.[93]

Ratiometric optical thermometry characteristics

Motivated by the strong thermal variation of the excitation spectra of **EuAg**, **Er@EuAg**, and **Yb@EuAg** (Fig. 4c, d, 5, 6 and S29, S30), we performed a thorough analysis in the context of their application as a source of ratiometric luminescent thermometry.[94] Testing various possible combinations of excitation peaks that could be used to construct a suitable thermometric parameter for the ratiometric detection of temperature, we focused our attention on three types of peaks: (i) a broad ligand-centered excitation band below 300 nm, as it increased strongly upon cooling, (ii) a series of distinct peaks in the 350–400 nm range (except those described in (iii) below), assignable to direct f–f excitation, which also significantly, yet more weakly, increased upon cooling, and (iii) the well-separated band in the 380–390 nm range, which revealed the oppo-

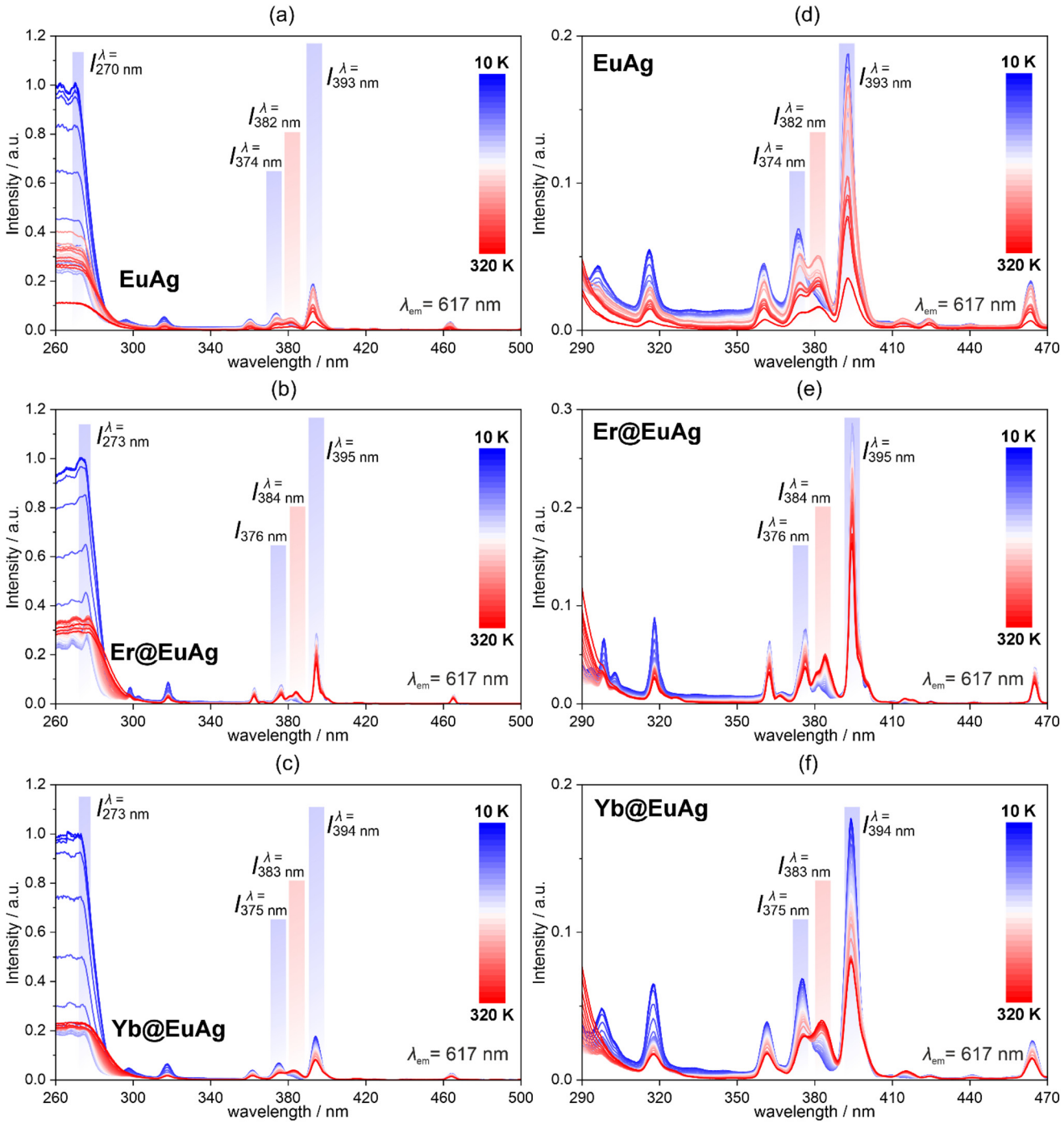

Fig. 5 Temperature-variable excitation spectra of **EuAg** (a and d), **Er@EuAg** (b and e) and **Yb@EuAg** (c and f) for the emission maximum at 617 nm (a–c), shown together with an enlargement of the 290–470 nm range (d–f). Marked areas represent the related ratiometric luminescence thermometry exploring the intensities at the maxima of selected excitation peaks (Fig. 6 and S30), red areas in (a–f) indicate peaks with intensities that are used as denominators in the definition of the Δ parameters, while the blue areas indicate peaks with intensities that are used as numerators (all these peaks are also labelled).

site T-dependence, as it was related to hot f–f electronic transitions (Fig. 5a–c, see also the discussion in the previous section). As a result of our preliminary testing, we decided to construct three different thermometric parameters, namely Δ_1, Δ_2, and Δ_3 (Fig. 5, 6, and S30). All of them were defined as the ratio between the intensities of two selected peaks at their maxima. For all these parameters, as a denominator, we employed the intensity of the excitation peak related to the hot band lying in the 380–390 nm range. As this peak undergoes a cooling-induced decrease in intensity, which is very different

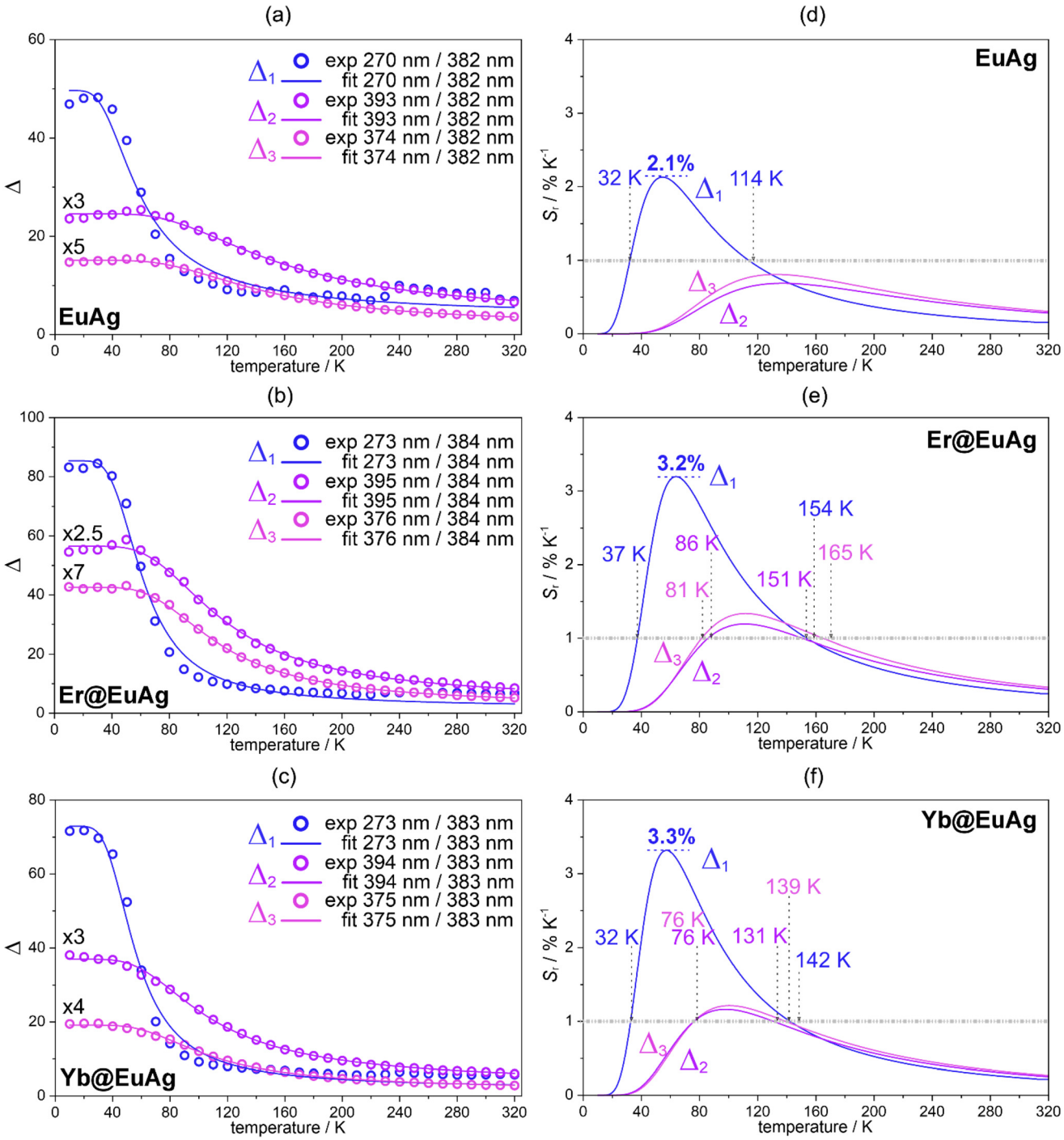

Fig. 6 Representative characteristics of the ratiometric luminescence thermometry of **EuAg** (a), **Er@EuAg** (b) and **Yb@EuAg** (c), exploring the intensities at the maxima of selected excitation peaks (Fig. 5), including the thermometric calibration curves, $\Delta(T)$, for **EuAg** (a), **Er@EuAg** (b) and **Yb@EuAg** (c), and the relative thermal sensitivity curves, $S_r(T)$, for **EuAg** (d), **Er@EuAg** (e) and **Yb@EuAg** (f). Empty circles in (a–c) are experimental data points, whereas solid curves represent the best fits using a Mott–Seitz model (eqn (5)). Best-fit parameters are gathered in Table S22. Dashed lines in (d–f) represent the boundary of an arbitrary criterion for optical thermometers that perform well ($S_r > 1\%\ K^{-1}$, $\delta T < 1$ K). Related temperature ranges of good thermometric performance are indicated by the boundary temperatures. The maximal thermal sensitivity for each compound is also marked in parts (d, e and f).

from all other peaks used, this approach ensures the optimized thermometric characteristics. For Δ_1, as a numerator, we employed the intensity of the ligand-centered excitation, while for the other two parameters, Δ_2 and Δ_3, we used two peaks related to the direct f–f excitation, centered at *ca.* 375 and 395 nm, respectively. The set of thermometric parameters

defined as such was plotted against T and fitted by using a single-exponential Mott–Seitz model, as expressed by eqn (4):

$$\Delta(T) = \frac{\Delta_0}{1 + \alpha \cdot \exp\left(\frac{-\Delta E}{k_B T}\right)} \quad (4)$$

where Δ_0 is the thermometric parameter at T = 0 K, α is the ratio of non-radiative and radiative rates, and ΔE is the activation energy barrier for the non-radiative relaxation channel.[46–50,94] The resulting best-fit curves are shown in Fig. 6a–c. Using the fitted $\Delta(T)$ dependences, in the next step, the relative thermal sensitivities, S_r, were determined by using eqn (5):[94]

$$S_r = \frac{1}{\Delta}\left|\frac{\delta\Delta}{\delta T}\right| \quad (5)$$

The resulting temperature dependences of S_r values are shown in Fig. 6d–f. Moreover, the temperature uncertainties at a given temperature, δT, were evaluated using the square roots of sums of squares of intensity uncertainties, taken directly from experimental data (Fig. S30 and Tables S22, S23, and the related comment in the SI).[46–50,94] For **EuAg**, the optimal Δ parameter is related to the intensity ratio between the ligand-centered excitation at 270 nm and the hot direct f–f excitation band at 382 nm (Δ_1). It ensured a maximal S_r value of 2.1% K^{-1} at 55 K and the high performance (*i.e.*, with S_r above 1% K^{-1})[46–50,94] thermometric response in the 32–114 K range. Thus, **EuAg** appears to be an effective ratiometric optical thermometer in the cryogenic temperature range below *ca.* 115 K (Fig. 6d). The other two Δ parameters, based on the direct f–f excitation (Δ_2 and Δ_3), *i.e.*, its cold and hot electronic transitions, indicate a distinct thermometric response in the higher temperature range from *ca.* 80 to 320 K. In particular, they work better than Δ_1 in the close-to-room-temperature range of 150–300 K. However, the maximal accessible S_r values are much worse than that for Δ_1, and the criterion for high-performance optical thermometry of 1% K^{-1} is not reached, even for the maximal sensitivity occurring at *ca.* 140 K (Fig. 6d). Similar trends are observed upon the incorporation of Er(III) and Yb(III) centers into **Er@EuAg** and **Yb@EuAg**, respectively (Fig. 6e and f). However, all the thermometric characteristics, including those relying on the ligand-centered excitation and those exploring only the direct f–f excitation routes (Fig. 5 and 6), are significantly improved in comparison to **EuAg**. For Δ_1, while the overall T-range of the optical thermometric response remains similar to that in **EuAg**, the maximal S_r value increases up to 3.2% K^{-1} at 64 K and 3.3% K^{-1} at 57 K for **Er@EuAg** and **Yb@EuAg**, respectively. Moreover, the T-ranges of high-performance optical thermometry broaden, mainly towards higher temperatures, to 37–154 K and 32–142 K for **Er@EuAg** and **Yb@EuAg**, respectively. Thermometry based on the cold and hot electronic transitions of direct f–f excitation is also improved after lanthanide mixing. As a result, the related maximal S_r values exceed the boundary of high-performance optical thermometry, reaching, for Δ_2, 1.34% K^{-1} at 111 K and 1.19% K^{-1} at 111 K for **Er@EuAg** and **Yb@EuAg**, respectively, while, for Δ_3, the respective limits are 1.22% K^{-1} at 101 K and 1.64% K^{-1} at 98 K. The resulting T-ranges of high-performance optical thermometry appear in the 81–165 K (Δ_2) and 86–151 K (Δ_3) regions, and the 76–142 K (Δ_2) and 76–131 K (Δ_3) regions, for **Er@EuAg** and **Yb@EuAg**, respectively (Fig. 6d–f and Table S23).

The observed thermometric responses for all three compounds discussed were found to be perfectly repeatable over three cycles of heating and cooling (Fig. S30). Therefore, it can be stated that high-performance ratiometric luminescent thermometry was generated for **EuAg**, with the further distinct improvement of this property upon the addition of Er(III) and Yb(III) centers in **Er@EuAg** and **Yb@EuAg**, respectively. To rationalize this effect, we plotted the experimental energy level diagram, indicating the main electronic transitions involved in optical thermometry (Fig. 7). The Δ_1 thermometry takes advantage of two optical effects showing opposite T-variation, *i.e.*, (i) the ligand-centered excitation undergoing the cooling-induced efficiency improvement, most probably due to quenching of the disturbing back energy transfer, and (ii) direct f–f excitation through a hot electronic transition from the lowest-lying excited $^7F_1$ multiplet undergoing cooling-induced weakening

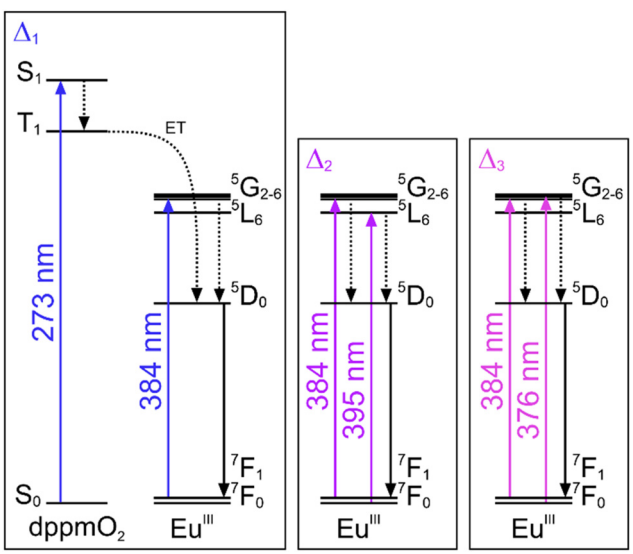

Fig. 7 Experimentally determined energy level diagram of **Er@EuAg** representing the electronic transitions explored for ratiometric optical thermometry, including three thermometric parameters employed based on selected peaks of the excitation spectra for the Eu(III) emission monitored (Δ_1, Δ_2, and Δ_3; see Fig. 5 for related spectra and thermometry characteristics). In each case, the electronic transitions responsible for the excitation peaks employed are indicated by colored arrows. Subsequent electronic transitions are indicated by arrows with black dotted lines (including ET = energy transfer from the organic ligand to the Eu(III) centers). The final emission monitored is indicated by arrows with black solid lines. The electronic states of embedded Er(III) centers are not shown for clarity. The energy level diagrams for **EuAg** and **Yb@EuAg** are almost identical, with only subtle differences in related wavelengths of less than 3 nm (Fig. 5).

due to the thermal depopulation of this excited level. The other two thermometric approaches are also based on the hot band intensity, but they are confronted with other bands of direct f–f excitation, which undergo cooling-induced intensity enhancement, most probably due to the quenching of non-radiative relaxation pathways related to the vibrational states of the molecular system. This mechanism also supports Δ_1 thermometry. Thus, as a result of the conjunction of three advantageous effects, *i.e.*, cooling-induced improvements of ligand-centered excitation through limiting (a) the back ET and (b) vibrational PL quenching, and (c) cooling-induced quenching of hot-band excitation, Δ_1 thermometry works best within the whole series of materials obtained.

A separate discussion should be devoted to the reasons for the improved optical thermometry upon the addition of Er(III) and Yb(III) centers to the Eu(III)–Ag(I) molecular matrix. Two main effects can rationalize this behavior. First, the incorporation of Er(III) and Yb(III) centers of a smaller size in comparison to Eu(III) centers forces the latter to adopt slightly smaller metric parameters. This structural restraint appears mainly for the Eu(III) centers that are neighboring the Er/Yb complexes. Even though this effect is expected to be rather minor due to the small amount of heavy 4f metal ions incorporated (as depicted, *e.g.*, by the extremely small energy shift of a single emission band corresponding to the highest-energy Eu(III) electronic transition of $^5D_0 \rightarrow {}^7F_0$, Fig. S56), it can lead to subtly shorter distances between the Eu(III) centers and the $dppmO_2$ ligand. This enables a better efficiency of ligand-to-metal energy transfer, which is achieved at the lowest temperatures, when all the quenching effects are cancelled out. As a result, the highest accessible Δ_1 parameter increases from **EuAg** (*ca.* 50) to **Er@EuAg** (*ca.* 85) and **Yb@EuAg** (*ca.* 73); this contributes to the overall stronger $\Delta_1(T)$ dependence in the latter compounds (Fig. 6a–c and Table S22). However, this effect cannot be the exclusive reason for the improved thermometry in **Er@EuAg** and **Yb@EuAg**, as the thermometric response, exploring only the direct f–f excitation (Δ_2 and Δ_3), is also enhanced in the mixed-lanthanide compounds. In this context, the other effect can be considered. The addition of Er(III) and Yb(III) centers of smaller sizes to the Eu(III) one leads to the structural distortion of Eu(III) complexes, especially those in their vicinity in the crystal structure. This is partially visible in bond lengths and angles in the SC-XRD data for **EuAg**, **Er@EuAg**, and **Yb@EuAg** (Tables S2, S5, and S6), even though they are average values, as two co-existing lanthanide centers are crystallographically indistinguishable in mixed-Ln compounds. Therefore, it can be deduced that the distortion of Eu(III) centers appears, and this effect presumably depends on the detailed molecular environment in the crystal lattice, *i.e.*, the presence of Er/Yb centers in their vicinity. As a result, the increased dispersion of related phonon modes is expected. This includes the vibrational states responsible for the thermally-induced emission quenching that is crucial for optical thermometry. The stronger temperature dependence then appears both for the excitation through the cold electronic transition as well as for the excitation through hot bands. As their *T*-dependences are opposite, this is expected to lead to the stronger *T*-dependence of related thermometric parameters, providing better performance of related optical thermometry.

To support the statement on the changes in the phonon mode scheme of the crystal lattice of **EuAg** occurring upon the addition of even small amounts of Er(III) and Yb(III) centers to **Er@EuAg** and **Yb@EuAg**, we performed additional IR spectral measurements on related polycrystalline samples, using an ATR-FTIR spectrometer (Fig. S46 and S47). We also performed these measurements for **ErAg** and **YbAg** to provide reliable reference data. In the wavenumber ranges related to organic ligands (*e.g.*, P=O group vibrations), cyanido linkers (*i.e.*, cyanido stretching vibrations), as well as bonds between lanthanide centers and donor atoms, one can notice distinct differences between **EuAg** and the pair of **ErAg** and **YbAg**, which are based on much smaller lanthanide ions. In contrast, in general, the IR spectra for **Er@EuAg** and **Yb@EuAg** are very similar to those detected for **EuAg**, which is not surprising, as the doping level of smaller-sized 4f metal ions is low. However, the low-energy components for the groups of absorption bands assignable to the cyanido stretching vibrations appear upon the addition of Er(III) or Yb(III) to **EuAg** (Fig. S47d). Moreover, there are subtle but noticeable differences in the low-energy part of the spectrum, *i.e.*, 400–480 cm^{-1}, which is assignable to the lanthanide–(donor atom) vibrations (Fig. S47f). This includes broadening of the band at *ca.* 470 cm^{-1}, the energy shift for the bands at *ca.* 418 and 446 cm^{-1}, and even the appearance of weak additional peaks at *ca.* 425 and 458 cm^{-1}. This confirms that the Er(III) and Yb(III) dopants generate changes in the phonon mode schemes of the crystal lattice of the **EuAg** host, which can affect optical thermometry, as stated above. It should be additionally noted that the changes in the vibrational states appear both for the cyanido-based skeleton and for the lanthanide metal complexes. This suggests that the influence of the dopants is not only local, *i.e.*, related to the changes in the vibrations strictly localized on the lanthanide complexes, but is spread over the whole framework. Thus, the applied dopants seem to be able to influence the long-range interactions between the molecular components embedded in the crystal lattice, which makes the associated changes in ratiometric optical thermometry very pronounced.

For further elucidation of the main factors responsible for enhanced optical thermometry upon the insertion of Er(III) and Yb(III) dopants into the **EuAg** framework, we performed additional *ab initio* calculations of the SA-CASSCF type, using an identical procedure to that described above for Eu(III) complexes in **EuAg** (see the related discussion above, Fig. 4, and comments on Fig. S22–S27 and Tables S12–S21 for details). These calculations were again performed for crucial emissive Eu(III) complexes but artificially embedded on the lanthanide position in the **ErAg** and **YbAg** compounds. As a result, we could get insights into the changes in the electronic structure of emissive Eu(III) centers upon the addition of Er(III) and Yb(III), affecting the geometry and metric parameters of the

lanthanide site of the structure, using the boundary case of the coordination sphere adopted by **ErAg** and **YbAg** analogs. This selection of structures for calculations was done to better illustrate the trend in the changes of the electronic structure, even though it was expected that the dopants in **Er@EuAg**, and **Yb@EuAg** would exhibit the limited strength of this effect due to the dominant amount of Eu(III) centers, thus geometries and metric parameters of lanthanide complexes are closer to those of **EuAg**. The resulting calculated energy splitting schemes for the $^7F_{0-5}$ and $^5D_0$ terms of Eu(III) complexes (Table S34) indicate that the change of the solid matrix from the original **EuAg** framework to the **ErAg** and **YbAg** ones affects the energies of all electronic multiplets. Some of the m_J levels within the terms reveal increased energies, while others decreased, without a general trend. These changes are rather small, up to *ca.* 40 cm^{-1}, which agrees well with the high level of similarity in the energies of the emission and excitation bands of **EuAg**, **Er@EuAg**, and **Yb@EuAg**, including their detailed splitting (Fig. 4 and S27, S29, S58). However, even such subtle changes in the energies of electronic states might contribute to the variation of optical thermometry, in particular, in the first of the abovementioned mechanisms related to ligand-to-metal energy transfer, which is known to be very sensitive to the energies of both the donor and acceptor states.[92–94] In this context, it is worth noting the distinct increase in the calculated energy of the emissive $^5D_0$ state upon the addition of Er(III) centers, which can contribute well to the highest Δ_1 parameter for **Er@EuAg** accessible at the lowest temperatures. The non-negligible variation in energy splitting, such as changes in the energies of the m_J levels within the multiplets, can also affect thermometry solely utilizing the hot and cold electronic transitions within the direct f–f excitation. However, a detailed analysis is precluded as the excitation spectra are used for thermometry and they correspond to the high-lying electronic states, which are beyond the scope of SA-CASSCF calculations with our computing resources. Nevertheless, as all the lower-lying excited states appeared to be altered by changes to the host framework, it can be extrapolated that the key $^5G_{2-6}$ and $^5L_6$ multiplets will also be modified at least to some extent, affecting the related optical thermometry (Fig. 7).

The remaining question regarding the influence of the Er(III) and Yb(III) dopants in the **EuAg** host framework is whether this impact is dominated by modulation of the short-range effects, including modification of the close vicinity of Eu(III) centers, the geometry/symmetry of these complexes, and their interaction with coordinated ligands or the modulation of long-range interactions within the crystalline molecular solid. This question, especially important from the viewpoint of the application of this approach in the next generation of related materials, could be addressed by employing the Judd–Ofelt (JO) theory.[96,97] Using the set of emission spectra of **EuAg**, **Er@EuAg**, and **Yb@EuAg** at selected temperatures, we calculated the crucial JO parameters of Ω_2 and Ω_4, and visualized their temperature dependences (Table S33 and Fig. S57, with the related comment, in the SI). For all three materials, the Ω_2 parameter, which represents the short-range interactions related to the close vicinity of emissive centers (*e.g.*, covalency of the ligand, asymmetry of the complex, and its other metric parameters), is found to distinctly change with temperature, especially above 60 K. Thus, this variation can contribute to the observed optical thermometry effect in the reported series of compounds. However, there are negligibly small differences in the Ω_2 values between the compounds, indicating that the short-range effects do not play the primary role in the enhancement of Eu(III)-based optical thermometry upon the addition of Er(III) and Yb(III) dopants. In contrast, the Ω_4 parameter, which represents the long-range interactions between the molecular components within the solid, including the modulated packing of the components, is found to differ significantly within the discussed series of **EuAg**, **Er@EuAg**, and **Yb@EuAg** (Fig. S57). In general, this parameter also depends distinctly on temperature, which suggests its significant impact on optical thermometry. Interestingly, the strongest temperature variation is observed for **EuAg**, whereas the Er(III) and Yb(III) dopants induce not only modified values of this JO parameter but also weaken its temperature dependence. Thus, it appears that the short-range interactions ensure a contribution to the optical thermometry that is not dependent on the dopants; this is similar across the series of reported compounds. Simultaneously, even though the long-range interactions might not play a dominant role in optical thermometry, they are much more sensitive to the dopants, becoming the major reason for the enhanced optical thermometry performance in **Er@EuAg** and **Yb@EuAg**.

All the above-discussed findings prove the beneficial role of Er(III) and Yb(III) centers in achieving more efficient optical thermometry in the reported compounds. It should be noted that the amount of Er/Yb admixtures cannot be large, as it can lead to the quenching of overall PL through their excited f–f states. However, this does not happen significantly for the reported cases of **Er@EuAg** and **Yb@EuAg**, as indicated by PL QYs that are found to decrease only subtly, from *ca.* 55.4% (**EuAg**) to 54.1–54.5% in the mixed-Ln compounds (Table S28).

Conclusions

We report a novel strategy for achieving the combination of molecular nanomagnetism and luminescent thermometry in a single-phase material; this relies on the incorporation of the magnetically anisotropic Ln(III) centers, shown for the Er(III) and Yb(III) complexes as examples, in a nearly diamagnetic but photoluminescent Eu(III)-based molecular matrix. We found that the Er(III) and Yb(III) centers linked with organic O,O-bidentate bis(diphenylphosphino)methane dioxide ligands ($dppmO_2$) and anionic dicyanidoargentate(I) metalloligands formed coordination chains in which substantial magnetic anisotropy of the 4f metal ions was induced. As a result, the SMM features are observed for the aforementioned lanthanide (III) centers. Alternatively, identical chain materials were obtained for red-emissive Eu(III) centers, which resulted in the

Eu(III)–Ag(I) luminescent material revealing a good room-temperature emission quantum yield of *ca.* 55% and ratiometric optical thermometry based on the excitation spectra. This optical thermometry takes advantage of the thermally modulated ligand-centered excitation, which is confronted with direct f–f excitation pathways, especially those related to hot f–f electronic transitions, providing the opposite temperature dependence. Thanks to this combined approach, high-performance optical thermometry was achieved in the cryogenic temperature range below *ca.* 115 K, with a maximal thermal sensitivity of up to 2.1% K^{-1} at 55 K. By linking the two above-presented findings, the SMM features for Er(III)/Yb(III)–Ag(I) compounds with good ratiometric optical thermometry in the Eu(III)–Ag(I) analog, we prepared mixed-lanthanide compounds of Er(III)–Eu(III)–Ag(I) and Yb(III)–Eu(III)–Ag(I) bearing small, *i.e.*, up to *ca.* 5%, admixtures of Er(III)/Yb(III) centers. This strategy resulted in f–f′–d heterometallic assemblies that combined SMM features related to the Er(III)/Yb(III) centers with the ratiometric optical thermometry related to the Eu(III) sides. This is the basis of a novel approach for an SMM-based optical thermometer.

We prove that the insertion of magnetic lanthanide centers, which do not have to be emissive, into the Eu(III)-based coordination framework generates SMMs, the temperature of which can be detected by examining the optical signal from the Eu(III) centers placed in their vicinity at the molecular scale. Moreover, this approach provides the simultaneous improvement of both magnetic and optical properties when compared with the mono-lanthanide analogs. The SMM features are enhanced, especially for the case of Er(III), by the magnetic dilution effect, leading to the quenching of quantum tunneling of magnetization. Ratiometric optical thermometry is greatly enhanced upon the addition of Er(III)/Yb(III) centers to the Eu(III)-based compound, as depicted by the increase of the maximal relative thermal sensitivity up to 3.2–3.2% K^{-1} and the broadening of the thermometry operating range from 32–114 K in the Eu(III)–Ag(I) system to 37–154 K and 32–142 K for the analogs with admixtures of Er(III) and Yb(III), respectively. These observations indicate the benefits of the approach presented, which is worth exploring with visible-light-emitting magnetically anisotropic lanthanide centers, such as Dy(III) or Tb(III), that can ensure better SMM characteristics as well as stronger entanglement between their luminescence and that of Eu(III). This further exploration and optimization of the reported approach can then be directed towards searching for the generation and detection of the strong interaction between the SMM features and optical thermometry, which is now one of the challenges of related research fields.[98] The other advantage of the approach presented is its modular characteristic, especially the employment of the $dppmO_2$ ligand, which can be functionalized thanks to its acidic C–H group.[85,86] Therefore, our work opens the perspective for more extended multifunctionality, *e.g.*, chirality and related chiroptical and magneto-chiral effects,[16] of such f–f′–d coordination systems, already working as SMM-based optical thermometers.

Conflicts of interest

There are no conflicts to declare.

Data availability

The data that support this article have been included in the supplementary information (SI). Supplementary information: experimental section; IR spectra; TG curves; detailed structural parameters; additional structural views; results of continuous shape measurement analysis; P-XRD patterns; SEM-EDXMA results; direct-current (dc) magnetic properties; complete alternating-current (ac) magnetic characteristics and the results of the additional fitting of the field- and temperature-dependences of magnetic relaxation times; description of syntheses and physicochemical characterization of Y(III)-diluted **ErAg** and **YbAg** compounds, and their magnetic properties; solid-state UV-vis absorption spectra; complete results of temperature-variable photoluminescent studies; results of *ab initio* calculations related to the magnetic and optical properties of the compounds obtained; calculated Judd–Ofelt parameters based on the emission spectra at various temperatures. See DOI: **https://doi.org/10.1039/d5qi02034d**.

The other supporting data can be obtained from the corresponding author upon reasonable request.

CCDC 2454863 (**EuAg**), 2454864 (**ErAg**), 2454865 (**YbAg**), 2454866 (**Er@EuAg**), and 2454867 (**Yb@EuAg**) contain the supplementary crystallographic data for this paper.[99a–e]

Acknowledgements

This work was financed by the National Science Center of Poland, the OPUS-21 project (2021/41/B/ST5/02544). The study was partly carried out using the research infrastructure cofunded by the European Union in the framework of the Smart Growth Operational Program, Measure 4.2; grant no. POIR.04. 02.00-00-D001/20, "ATOMIN 2.0 – ATOMic scale science for the INnovative economy". The authors gratefully acknowledge a DUS grant from the Faculty of Chemistry under the Strategic Programme Excellence Initiative at Jagiellonian University.

References

1 L. N. Quan, B. P. Rand, R. H. Friend, S. G. Mhaisalkar, T.-W. Lee and E. H. Sargent, Perovskites for Next-Generation Optical Sources, *Chem. Rev.*, 2019, **110**, 7444–7477.
2 M. D. Allendorf, R. Dong, X. Feng, S. Kaskel, D. Matoga and V. Stavila, Electronic Devices Using Open Framework Materials, *Chem. Rev.*, 2020, **120**, 8581–8640.
3 G.-H. Lee, H. Moon, H. Kim, G. H. Lee, W. Kwon, S. Yoo, D. Myung, S. H. Yun, Z. Bao and S. K. Hahn, Multifunctional materials for implantable and wearable

photonic healthcare devices, *Nat. Rev. Mater.*, 2020, **5**, 149–165.
4 S. Bellani, A. Bartolotta, A. Agresti, G. Calogero, G. Grancini, A. Di Carlo, E. Kymakis and F. Bonaccorso, Solution-processed two-dimensional materials for next-generation photovoltaics, *Chem. Soc. Rev.*, 2021, **50**, 11870–11965.
5 S. Fop, Solid oxide proton conductors beyond perovskites, *J. Mater. Chem. A*, 2021, **9**, 18836–18856.
6 X.-D. Huang, G.-H. Wen, S.-S. Bao, J.-G. Jia and L.-M. Zheng, Thermo- and light-triggered reversible interconversion of dysprosium–anthracene complexes and their responsive optical, magnetic and dielectric properties, *Chem. Sci.*, 2021, **12**, 929–937.
7 K. Du, J. Feng, X. Gao and H. Zhang, Nanocomposites based on lanthanide-doped upconversion nanoparticles: diverse designs and applications, *Light: Sci. Appl.*, 2022, **11**, 222.
8 J. Liu and T. Hesjedal, Magnetic Topological Insulator Heterostructures: A Review, *Adv. Mater.*, 2023, **35**, 2102427.
9 X.-D. Huang, X.-F. Ma and L.-M. Zheng, Photo-responsive Single-Molecule Magnet Showing 0D to 1D Single-Crystal-to-Single-Crystal Structural Transition and Hysteresis Modulation, *Angew. Chem., Int. Ed.*, 2023, **63**, e202300088.
10 S. Dutta, L. Nego and P. Munschi, Multifunctional single-component organic molecular materials: ferroelectricity, negative thermal expansion, and polymorphism, *Mater. Adv.*, 2024, **5**, 7495–7515.
11 P.-H. Guo, J.-L. Liu, J.-H. Jia, J. Wang, F.-S. Guo, Y.-C. Chen, W.-Q. Lin, J.-D. Leng, D.-H. Bao, X.-D. Zhang, J.-H. Luo and M.-L. Tong, Multifunctional Dy^{III}_4 Cluster Exhibiting White-Emitting, Ferroelectric and Single-Molecule Magnet Behavior, *Chem. – Eur. J.*, 2013, **19**, 8769–8773.
12 M. Estrader, J. Salinas Uber, L. A. Barrios, J. Garcia, P. Lloyd-Williams, O. Roubeau, S. J. Teat and G. Aromí, A Magneto-optical Molecular Device: Interplay of Spin Crossover, Luminescence, Photomagnetism, and Photochromism, *Angew. Chem., Int. Ed.*, 2017, **56**, 15622–15627.
13 N. A. Spaldin and R. Ramesh, Advances in magnetoelectric multiferroics, *Nat. Mater.*, 2019, **18**, 203–212.
14 R. Marin, G. Brunet and M. Murugesu, Shining New Light on Multifunctional Lanthanide Single-Molecule Magnets, *Angew. Chem., Int. Ed.*, 2021, **60**, 1728–1746.
15 R. Jankowski, M. Wyczesany and S. Chorazy, Multifunctionality of luminescent molecular nanomagnets based on lanthanide complexes, *Chem. Commun.*, 2023, **59**, 5961–5986.
16 J. J. Zakrzewski, M. Liberka, J. Wang, S. Chorazy and S. Ohkoshi, Optical Phenomena in Molecule-Based Magnetic Materials, *Chem. Rev.*, 2024, **124**, 5930–6050.
17 S.-D. Zhu, Y.-L. Zhou, Y. Lei, H.-R. Wen, S.-J. Liu, C.-M. Liu, S.-Y. Zhang and Y.-B. Lu, Combined performance of circularly polarized luminescence and proton conduction in homochiral cadmium(II)–terbium(III) complexes, *Inorg. Chem. Front.*, 2024, **11**, 1531–1539.
18 C. A. Mattei, V. Montigaud, B. Lefeuvre, V. Dorcet, G. Argouarch, O. Cador, B. Le Guennic, O. Maury, C. Lalli, Y. Guyot, S. Guy, C. Gindre, A. Bensalah-Ledoux, F. Riobé, B. Baguenard and F. Pointillart, Circularly polarized luminescence in the one-dimensional assembly of binaphtyl-based Yb(III) single-molecule magnets, *J. Mater. Chem. C*, 2023, **11**, 7299–7310.
19 M. S. Raju, K. Dhbaibi, M. Grasser, V. Dorcet, I. Breslavetz, K. Paillot, N. Vanthuyne, O. Cador, G. L. J. A. Rikken, B. Le Guennic, J. Crassous, F. Pointillart, C. Train and M. Atzori, Magneto-Chiral Dichroism in a One-Dimensional Assembly of Helical Dysprosium(III) Single-Molecule Magnets, *Inorg. Chem.*, 2023, **62**, 17583–17587.
20 D. A. Gálico and M. Murugesu, Toward Magneto-Optical Cryogenic Thermometers with High Sensitivity: A Magnetic Circular Dichroism Based Thermometric Approach, *Angew. Chem., Int. Ed.*, 2023, **62**, e202309152.
21 L. C. Adi, O. G. Willis, A. Gabbani, G. L. J. A. Rikken, L. Di Bari, C. Train, F. Pineider, F. Zinna and M. Atzori, Magneto-Chiral Dichroism of Chiral Lanthanide Complexes in the Context of Richardson's Theory of Optical Activity, *Angew. Chem., Int. Ed.*, 2024, **63**, e202412521.
22 D. A. Gálico and M. Murugesu, Magnetic Circularly Polarized Luminescence with Heterometallic Molecular Cluster-Aggregates, *Adv. Opt. Mater.*, 2024, **12**, 2401064.
23 B. P. Bloom, Y. Paltiel, R. Naaman and D. H. Waldeck, Chiral Induced Spin Selectivity, *Chem. Rev.*, 2024, **124**, 1950–1991.
24 R. Sessoli, D. Gatteschi, A. Caneschi and M. A. Novak, Magnetic bistability in a metal-ion cluster, *Nature*, 1993, **365**, 141–143.
25 L. Bogani and W. Wernsdorfer, Molecular spintronics using single-molecule magnets, *Nat. Mater.*, 2008, **7**, 179–186.
26 E. Coronado, Molecular magnetism: from chemical design to spin control in molecules, materials and devices, *Nat. Rev. Mater.*, 2020, **5**, 87–104.
27 F. Houard, Q. Evrard, G. Calvez, Y. Suffren, C. Daiguebonne, O. Guillou, F. Gendron, B. Le Guennic, T. Guizouarn, V. Dorcet, M. Mannini and K. Bernot, Chiral Supramolecular Nanotubes of Single-Chain Magnets, *Angew. Chem., Int. Ed.*, 2020, **59**, 780–784.
28 J. H. Mecchia, D. Cabrosi, L. M. Carrella, E. Rentschler and P. Albores, SMM Behaviour of the Butterfly $\{Cr^{III}_2Dy^{III}_2\}$ Pivalate Complex and Magneto-structurally Correlated Relaxation Thermal Barrier, *Chem. – Eur. J.*, 2022, **28**, e202201450.
29 V. Vieru, S. Gomez-Coca, E. Ruiz and L. F. Chibotaru, Increasing the Magnetic Blocking Temperature of Single-Molecule Magnets, *Angew. Chem., Int. Ed.*, 2024, **63**, e202303146.
30 A. S. Armenis, A. Mondal, S. R. Giblin, D. I. Alexandropoulos, J. Tnag, R. A. Layfield and T. C. Stamatatos, 'Kick-in the head': high-performance and air-stable mononuclear Dy^{III} single-molecule magnets with

pseudo-D_{6h} symmetry from a [1 + 1] Schiff-base macrocycle approach, *Inorg. Chem. Front.*, 2025, **12**, 1214–1224.
31 J. D. Rinehart and J. R. Long, Exploiting single-ion anisotropy in the design of f-element single-molecule magnets, *Chem. Sci.*, 2011, **2**, 2078–2085.
32 S. T. Liddle and J. van Slageren, Improving f-element single molecule magnets, *Chem. Soc. Rev.*, 2015, **44**, 6655–6669.
33 C. A. P. Goodwin, F. Ortu, D. Reta, N. F. Chilton and D. P. Mills, Molecular magnetic hysteresis at 60 kelvin in dysprosocenium, *Nature*, 2017, **548**, 439–442.
34 F.-S. Guo, B. M. Day, Y. Chen, M.-L. Tong, A. Mansikkamäki and R. A. Layfield, A Dysprosium Metallocene Single-Molecule Magnet Functioning at the Axial Limit, *Angew. Chem., Int. Ed.*, 2017, **56**, 11445–11449.
35 F.-S. Guo, B. M. Day, Y.-C. Chen, M.-L. Tong, A. Mansikkamäki and R. A. Layfield, Magnetic hysteresis up to 80 kelvin in a dysprosium metallocene single-molecule magnet, *Science*, 2018, **362**, 1400–1403.
36 C. A. Gould, K. R. McClain, D. Reta, J. G. C. Kragskow, D. A. Marchiori, E. Lachman, E.-S. Choi, J. G. Analytis, R. D. Britt, N. F. Chilton, B. G. Harvey and J. R. Long, Ultrahard magnetism from mixed-valence dilanthanide complexes with metal-metal bonding, *Science*, 2022, **375**, 198–202.
37 P. K. Sahu, S. Kapurwan and S. Konar, Epitome of polyoxotungstate-coordinated lanthanide-based single-molecule magnets, *Chem. Commun.*, 2025, **61**, 6105–6117.
38 K. Bernot, C. Daiguebonne, G. Calvez, Y. Suffren and O. Guillou, A Journey in Lanthanide Coordination Chemistry: From Evaporable Dimers to Magnetic Materials and Luminescent Devices, *Acc. Chem. Res.*, 2021, **54**, 427–440.
39 A. Tubau, L. Rodriguez, P. Pander, L. Weatherill, F. B. Dias, M. Font-Bardia and R. Vicente, Slow magnetic relaxation and luminescence properties in β-diketonate lanthanide (III) complexes. Preparation of Eu(III) and Yb(III) OLED devices, *J. Mater. Chem. C*, 2024, **12**, 8127–8144.
40 N. T. Anh Le, Y. Son, I. Kim, R. Tokunaga, S. Hayami and K. S. Min, Deuterium-Enhanced Photoluminescence and Magnetic Properties in Octanuclear Terbium(III) Complexes Containing a Hexadentate N_2O_4-Type Ligand, *Cryst. Growth Des.*, 2025, **25**, 2193–2205.
41 M. Boulon, G. Cucinotta, J. Luzon, C. Degl'Innocenti, M. Perfetti, K. Bernot, G. Calvez, A. Caneschi and R. Sessoli, Magnetic Anisotropy and Spin Parity Effect Along the Series of Lanthanide Complexes with DOTA, *Angew. Chem.*, 2013, **125**, 368–372.
42 Y. Bi, C. Chen, Y.-F. Zhao, Y.-Q. Zhang, S.-D. Jiang, B.-W. Wang, J.-B. Han, J.-L. Sun, Z.-Q. Bian, Z.-M. Wang and S. Gao, Thermostability and photoluminescence of Dy (III) single-molecule magnets under a magnetic field, *Chem. Sci.*, 2016, **7**, 5020–5031.
43 J. Long, Y. Guari, R. A. S. Ferreira, L. D. Carlos and J. Larionova, Recent advances in luminescent lanthanide based Single-Molecule Magnets, *Coord. Chem. Rev.*, 2018, **363**, 57–70.
44 J.-H. Jia, Q.-W. Li, Y.-C. Chen, J.-L. Liu and M.-L. Tong, Luminescent single-molecule magnets based on lanthanides: Design strategies, recent advances and magneto-luminescent studies, *Coord. Chem. Rev.*, 2019, **378**, 365–381.
45 A. G. Bispo-Jr, L. Yeh, D. Errulat, D. A. Gálico, F. A. Sigoli and M. Murugesu, Improving the performance of β-diketonate-based Dy^{III} single-molecule magnets displaying luminescence thermometry, *Chem. Commun.*, 2023, **59**, 8723–8726.
46 D. Errulat, R. Marin, D. A. Gálico, K. L. M. Harriman, A. Pialat, B. Gabidullin, F. Iikawa, O. D. D. Couto, J. O. Moilanen, E. Hemmer, F. A. Sigoli and M. Murugesu, A Luminescent Thermometer Exhibiting Slow Relaxation of the Magnetization: Toward Self-Monitored Building Blocks for Next-Generation Optomagnetic Devices, *ACS Cent. Sci.*, 2019, **5**, 1187–1198.
47 R. A. S. Ferreira, E. Mamontova, A. M. P. Botas, M. Shestakov, J. Vanacken, V. Moshchalkov, Y. Guari, L. F. Chibotaru, D. Luneau, P. S. André, J. Larionova, J. Long and L. D. Carlos, Synchronous Temperature and Magnetic Field Dual-Sensing by Luminescence in a Dysprosium Single-Molecule Magnet, *Adv. Opt. Mater.*, 2021, **9**, 202101495.
48 G. Brunet, R. Marin, M.-J. Monk, U. Resch-Genger, D. A. Gálico, F. A. Sigoli, E. A. Suturina, E. Hemmer and M. Murugesu, Exploring the dual functionality of an ytterbium complex for luminescence thermometry and slow magnetic relaxation, *Chem. Sci.*, 2019, **10**, 6799–6808.
49 J. Wang, J. J. Zakrzewski, M. Heczko, M. Zychowicz, K. Nakagawa, K. Nakabayashi, B. Sieklucka, S. Chorazy and S. Ohkoshi, Proton Conductive Luminescent Thermometer Based on Near-Infrared Emissive $\{YbCo_2\}$ Molecular Nanomagnets, *J. Am. Chem. Soc.*, 2020, **142**, 3970–3979.
50 J. Wang, J. J. Zakrzewski, M. Zychowicz, Y. Xin, H. Tokoro, S. Chorazy and S. Ohkoshi, Desolvation-Induced Highly Symmetrical Terbium(III) Single-Molecule Magnet Exhibiting Luminescent Self-Monitoring of Temperature, *Angew. Chem., Int. Ed.*, 2023, **62**, e202306372.
51 S. Zanella, M. Aragon-Alberti, C. D. S. Brites, F. Salles, L. D. Carlos and J. Long, Luminescent Single-Molecule Magnets as Dual Magneto-Optical Molecular Thermometers, *Angew. Chem., Int. Ed.*, 2023, **62**, e202306970.
52 J. Wang, J. J. Zakrzewski, M. Zychowicz, V. Vieru, L. F. Chibotaru, K. Nakabayashi, S. Chorazy and S. Ohkoshi, Holmium(III) molecular nanomagnets for optical thermometry exploring the luminescence re-absorption effect, *Chem. Sci.*, 2021, **12**, 730–741.
53 P. J. Bonarek, M. Zychowicz, J. Rzepiela, M. Liberka, S. Baś, J. J. Zakrzewski and S. Chorazy, Design of Dy^{III} single-molecule magnets with molecularly installed luminescent thermometers based on bridging $[Pt^{II}(CN)_2(C^N)]^-$ complexes, *Inorg. Chem. Front.*, 2024, **11**, 7966–7978.
54 M. Suta and A. Meijerink, A Theoretical Framework for Ratiometric Single Ion Luminescent Thermometers—

Thermodynamic and Kinetic Guidelines for Optimized Performance, *Adv. Theory Simul.*, 2020, **3**, 2000176.

55 M. A. Hernández-Rodríguez, C. D. S. Brites, G. Antorrena, R. Piñol, R. Cases, L. Pérez-García, M. Rodrigues, J. A. Plaza, N. Torras, I. Díez, A. Millán and L. D. Carlos, Lanthanide Luminescence to Mimic Molecular Logic and Computing through Physical Inputs, *Adv. Opt. Mater.*, 2020, **8**, 2000312.

56 S. Zanella, M. A. Hernández-Rodríguez, L. Fu, L. D. Carlos, R. A. S. Ferreira and C. D. S. Brites, Reprogrammable and Reconfigurable Photonic Molecular Logic Gates Based on Ln^{3+} Ions, *Adv. Opt. Mater.*, 2022, **10**, 2200138.

57 C. D. S. Brites, Enlightening molecular logic: basics, tools and techniques for newcomers, *Mater. Horiz.*, 2025, **12**, 4016–4026.

58 M. S. Raju, K. Paillot, I. Breslavetz, G. Novitchi, G. L. J. A. Rikken, C. Train and M. Atzori, Optical Readout of Single-Molecule Magnets Magnetic Memories with Unpolarized Light, *J. Am. Chem. Soc.*, 2024, **146**, 23616–23624.

59 M. Aragon-Alberti, H. Flichot, M. Gascoin, B. Le Guennic, O. Cador, G. Novitchi, G. L. J. A. Rikken, C. Train, F. Pointillart and M. Atzori, Magneto-Optical Readout of a Chiral Single-Molecule Magnet at Telecom Wavelengths, *J. Am. Chem. Soc.*, 2026, **148**, 67–72.

60 D. A. Galico and M. Murugesu, Dual-signalled magneto-optical barcodes with lanthanide-based molecular cluster-aggregates, *Nanoscale*, 2023, **15**, 18198–18202.

61 Y. Wu, Z.-Y. Ruan, C. Zhang, J.-N. Chen, X.-Y. Wang, Z. Chen, X. Gou, W. Lan, X.-J. Kong, J.-L. Liu, P. Cheng and W. Shi, Strong and Switchable Magneto-Optical Effect in Air-Stable Chiral Dy^{III} Complexes with Magnetic Anisotropy, *J. Am. Chem. Soc.*, 2025, **147**, 20799–20806.

62 T. P. Latendresse, V. Vieru, B. O. Wilkins, N. S. Bhuvanesh, L. F. Chibotaru and M. Nippe, Magnetic Properties of a Terbium–[1]Ferrocenophane Complex: Analogies between Lanthanide–Ferrocenophane and Lanthanide–Bis-phthalocyanine Complexes, *Angew. Chem., Int. Ed.*, 2018, **57**, 8164–8169.

63 F. Guegan, J. Jung, B. Le Guennic, F. Riobe, O. Maury, B. Gillon, J.-F. Jacquot, Y. Guyot, C. Morell and D. Luneau, Evidencing under-barrier phenomena in a Yb(III) SMM: a joint luminescence/neutron diffraction/SQUID study, *Inorg. Chem. Front.*, 2019, **6**, 3152–3157.

64 E. Castellanos, F. Benner and S. Demir, Linear, Electron-Rich Erbium Single-Molecule Magnet with Dibenzocyclooctatetraene Ligands, *Inorg. Chem.*, 2024, **63**, 9888–9898.

65 D. Cabrosi, J. H. Mecchia Ortiz, L. M. Carrella, E. Rentschler and P. Albores, SMM features of a large lanthanide family of butterfly $Cr^{III}{}_2Ln^{III}{}_2$ pivalate complexes (Ln = Gd, Tb, Dy, Ho, Er, Tm and Yb), *Dalton Trans.*, 2024, **53**, 12189–12198.

66 J. Emerson-King, G. K. Gransbury, B. E. Atkinson, W. J. A. Blackmore, G. F. S. Whitehead, N. F. Chilton and D. P. Mills, Soft magnetic hysteresis in a dysprosium amide–alkene complex up to 100 kelvin, *Nature*, 2025, **643**, 125–129.

67 J. J. Zakrzewski, B. Sieklucka and S. Chorazy, Europium(III) Photoluminescence Governed by d^8–d^{10} Heterometallophilic Interactions in Trimetallic Cyanido-Bridged Coordination Frameworks, *Inorg. Chem.*, 2020, **59**, 1393–1404.

68 Z. Cai, C. Wei, B. Sun, H. Wei, Z. Liu, Z. Bian and C. Huang, Luminescent europium(III) complexes based on tridentate isoquinoline ligands with extremely high quantum yield, *Inorg. Chem. Front.*, 2021, **8**, 41–47.

69 T. Fujii, Y. Kitagawa, Y. Hasegawa, H. Imoto and K. Naka, Emission Properties of Eu(III) Complexes Containing Arsine and Phosphine Ligands with Annulated Structures, *Inorg. Chem.*, 2022, **61**, 17662–17672.

70 J. Corredoira-Vazquez, C. Gonzalez-Barreira, M. Fondo, A. M. Garcia-Deibe, J. Sanmartin-Matalobos, S. Gomez-Coca, E. Ruiz, C. D. S. Brites and L. D. Carlos, An air-stable high-performance single-molecule magnet operating as a luminescent thermometer below its blocking temperature, *Inorg. Chem. Front.*, 2025, **12**, 5506–5516.

71 A. Carlotto, L. Babetto, S. Carlotto, M. Miozzi, R. Seraglia, M. Casarin, G. Bottaro, M. Rancan and L. Armelao, Luminescent Thermometers: From a Library of Europium (III) β-Diketonates to a General Model for Predicting the Thermometric Behaviour of Europium-Based Coordination Systems, *ChemPhotoChem*, 2020, **4**, 674–684.

72 Y. Yang, L. Li, H. Suo, P. Li, Z. Wang and Z. Zhang, Eu^{3+}-based dual-excitation single-emission luminescent ratiometric thermometry, *Opt. Express*, 2022, **30**, 265–274.

73 L. Blois, A. N. Carneiro-Neto, O. L. Malta and H. F. Brito, A theoretical framework for optical thermometry based on excited-state absorption and lifetimes of Eu^{3+} compounds, *J. Lumin.*, 2022, **249**, 119039.

74 A. Kourtellaris, W. Lafargue-Dit-Hauret, F. Massuyeau, C. Latouche, A. J. Tasiopoulos and H. Serier-Brault, Tuning of Thermometric Performances of Mixed Eu–Tb Metal–Organic Frameworks through Single-Crystal Coordinating Solvent Exchange Reactions, *Adv. Opt. Mater.*, 2022, **10**, 2200484.

75 V. Tangoulis, V. Nastopoulos, N. Panagiotou, A. Tasiopoulos, G. Itskos, M. Athanasiou, E. Moreno-Pineda, W. Wernsdorfer, M. Schulze and O. Malina, High-Performance Luminescence Thermometer with Field-Induced Slow Magnetic Relaxation Based on a Heterometallic Cyanido-Bridged 3d–4f Complex, *Inorg. Chem.*, 2022, **61**, 2546–2557.

76 K. Kumar, O. Stefańczyk, S. Chorazy, K. Nakabayashi, B. Sieklucka and S. Ohkoshi, Effect of Noble Metals on Luminescence and Single-Molecule Magnet Behavior in the Cyanido-Bridged Ln-Ag and Ln-Au (Ln = Dy, Yb, Er) Complexes, *Inorg. Chem.*, 2019, **58**, 5677–5687.

77 K. Kumar, G. Li, O. Stefanczyk, S. Chorazy, K. Nakabayashi and S. Ohkoshi, Slow magnetic relaxation in Nd(III) and Sm (III) complexes formed in three-dimensional lanthanide-dicyanidometallate(I) frameworks exhibiting luminescent properties, *J. Mater. Chem. C*, 2023, **11**, 1008–1020.

78 Z. Assefa, G. Shankle, H. H. Patterson and R. Reynolds, Photoluminescence Studies of Lanthanide Ion Complexes

of Gold and Silver Dicyanides: A New Low-Dimensional Solid-state Class for Nonradiative Excited-State Energy Transfer, *Inorg. Chem.*, 1994, **33**, 2187–2195.

79 J. C. F. Colis, R. Staples, C. Tripp, D. Labrecque and H. Patterson, Metallophilic Interactions in Closed-Shell d^{10} Metal-Metal Dicyanide Bonded Luminescent Systems Eu $[Ag_xAu_{1-x}(CN)_2]_3$ and Their Tunability for Excited State Energy Transfer, *J. Phys. Chem. B*, 2005, **109**, 102–109.

80 J.-C. G. Bünzli and C. Piguet, Taking advantage of luminescent lanthanide ions, *Chem. Soc. Rev.*, 2005, **34**, 1048–1077.

81 F. Artizzu, M. Atzori, J. Liu, D. Mara, K. Van Hecke and R. Van Deun, Solution-processable Yb/Er 2D-layered metal-lorganic frameworks with high NIR-emission quantum yields, *J. Mater. Chem. C*, 2019, **7**, 11207–11214.

82 Y. Jeong, N. T. Anh Le, J. Ju, I. Olshevskaia, D. Cho, R. Tokunaga, S. Hayami and K. S. Min, Near-infrared emissive mononuclear lanthanide(III) complexes based on chiral Schiff base ligands: synthesis, crystal structure, luminescence, and magnetic properties, *Dalton Trans.*, 2025, **54**, 14533–14564.

83 A. J. Brown, D. Pinkowicz, M. R. Saber and K. R. Dunbar, A Trigonal-Pyramidal Erbium(III) Single-Molecule Magnet, *Angew. Chem., Int. Ed.*, 2015, **54**, 5864–5868.

84 A. Mondal and S. Konar, Strong Equatorial Crystal Field Enhances the Axial Anisotropy and Energy Barrier for Spin Reversal Process in Yb_2 Single Molecule Magnets, *Chem. – Eur. J.*, 2021, **27**, 3449–3456.

85 Y.-Z. Pan, Q.-Y. Hua, L.-S. Lin, Y.-B. Qiu, J.-L. Liu, A.-J. Zhou, W.-Q. Lin and J.-D. Leng, A slowly magnetic relaxing Sm^{III} monomer with a D_{5h} equatorial compressed ligand field, *Inorg. Chem. Front.*, 2020, **7**, 2335–2342.

86 J.-D. Leng, Q.-Y. Hua, Q.-T. Liu, Z.-X. Tao, N.-W. Tan, Y.-F. Wang and W.-Q. Lin, Slow magnetic relaxation of mononuclear complexes based on uncommon Kramers lanthanide ions Ce^{III}, Sm^{III} and Yb^{III}, *Dalton Trans.*, 2022, **51**, 12661–12669.

87 G. Li Manni, I. F. Galván, A. Alavi, *et al.*, The OpenMolcas Web: A Community-Driven Approach to Advancing Computational Chemistry, *J. Chem. Theory Comput.*, 2023, **19**, 6933–6991.

88 M. Zychowicz, H. Dzielak, J. Rzepiela and S. Chorazy, Synergy of Experiment and Broadened Exploration of Ab Initio Calculations for Understanding of Lanthanide–Pentacyanido-cobaltate Molecular Nanomagnets and Their Optical Properties, *Inorg. Chem.*, 2024, **63**, 19213–19226.

89 C. V. Topping and S. J. Blundell, A.C. susceptibility as a probe of low-frequency magnetic dynamics, *J. Phys.: Condens. Matter*, 2019, **31**, 013001.

90 M. Liberka, M. Zychowicz, W. Zychowicz and S. Chorazy, Neutral dicyanidoferrate(II) metalloligands for the rational design of dysprosium(III) single-molecule magnets, *Chem. Commun.*, 2022, **58**, 6381–6384.

91 H. Lu, R. Yson, J. Ford, H. J. Tracy, A. B. Carrier, A. Keller, J. L. Mullin, M. J. Poissan, S. Sawan and H. H. Patterson, Tunable energy transfer from d^{10} heterobimetallic dicyanide(I) donor ions to terbium(III) acceptor ions in luminescent $Tb[Ag_xAu_{1-x}(CN)_2]_3$ ($x = 0 \rightarrow 1$), *Chem. Phys. Lett.*, 2007, **443**, 55–60.

92 J.-C. G. Bünzli, On the design of highly luminescent lanthanide complexes, *Coord. Chem. Rev.*, 2015, **293–294**, 19–47.

93 K. Binnemans, Interpretation of europium(III) spectra, *Coord. Chem. Rev.*, 2015, **295**, 1–45.

94 C. D. S. Brites, P. P. Lima, N. J. O. Silva, A. Millán, V. S. Amaral, F. Palacio and L. D. Carlos, Thermometry at the nanoscale, *Nanoscale*, 2012, **4**, 4799–4829.

95 I. E. Kolesnikov, A. A. Kalinchev, M. A. Kurochkin, D. V. Mamonova, E. Y. Kolesnikov and E. Lähderanta, Ratiometric Optical Thermometry Based on Emission and Excitation Spectra of YVO_4:Eu^{3+} Nanophosphors, *J. Phys. Chem. C*, 2019, **123**, 5136–5143.

96 M. P. Hehlen, M. G. Brik and K. W. Krämer, 50th anniversary of the Judd–Ofelt theory: An experimentalist's view of the formalism and its application, *J. Lumin.*, 2013, **136**, 221–239.

97 A. Ćirić, S. Stojadinović, M. Sekulić and M. D. Dramićanin, JOES: An application software for Judd-Ofelt analysis from Eu^{3+} emission spectra, *J. Lumin.*, 2019, **205**, 351–356.

98 M. Aragon-Alberti, M. Dyksik, C. D. S. Brites, J. Rouquette, P. Plochocka, L. D. Carlos and J. Long, Rethinking Assumptions: Assessing the Impact of Strong Magnetic Fields on Luminescence Thermometry, *J. Am. Chem. Soc.*, 2024, **146**, 33723–33731.

99 (*a*) CCDC 2454863: Experimental Crystal Structure Determination, 2026, DOI: **10.5517/ccdc.csd.cc2ndh4q**; (*b*) CCDC 2454864: Experimental Crystal Structure Determination, 2026, DOI: **10.5517/ccdc.csd.cc2ndh5r**; (*c*) CCDC 2454865: Experimental Crystal Structure Determination, 2026, DOI: **10.5517/ccdc.csd.cc2ndh6s**; (*d*) CCDC 2454866: Experimental Crystal Structure Determination, 2026, DOI: **10.5517/ccdc.csd.cc2ndh7t**; (*e*) CCDC 2454867: Experimental Crystal Structure Determination, 2026, DOI: **10.5517/ccdc.csd.cc2ndh8v**.